Cycling of lithogenic marine particles in the US GEOTRACES North Atlantic transect

Daniel C. Ohnemus [a,b,d,*], Phoebe J. Lam [b,c]

[a] MIT-WHOI Joint Program in Oceanography, Massachusetts Institute of Technology/Woods Hole Oceanographic Institution, Woods Hole, MA 02543, USA
[b] Department of Marine Chemistry and Geochemistry, Woods Hole Oceanographic Institution, Woods Hole, MA 02543, USA
[c] Ocean Sciences Department, University of California Santa Cruz, Santa Cruz, CA 95064, USA
[d] Bigelow Laboratory for Ocean Sciences, 60 Bigelow Drive, East Boothbay, ME, USA

A B S T R A C T

In this paper, we present, describe, and model the first size-fractionated (0.8–51 μm; > 51 μm) water-column particulate trace metal results from the US GEOTRACES North Atlantic Zonal Transect in situ pumping survey, with a focus on the lithogenic tracer elements Al, Fe and Ti. This examination of basin-wide, full-depth distributions of particulate elements elucidates many inputs and processes—some for bulk lithogenic material, others element-specific—which are presented via concentration distributions, elemental ratios, size-fractionation dynamics, and steady-state inventories. Key lithogenic inputs from African dust, North American boundary interactions, the Mediterranean outflow, hydrothermal systems, and benthic nepheloid layers are described. Using the refractory lithogenic tracer Ti, we develop a 1-D model for lithogenic particle distributions and test the sensitivities of size-fractionated open-ocean particulate Ti profiles to biotically driven aggregation, disaggregation rates, vertical sinking speeds, and dust input rates. We discuss applications of this lithogenic model to particle cycling in general, and to POC cycling specifically.

© 2014 The Authors. Published by Elsevier Ltd. This is an open access article under the CC BY-NC-ND license (http://creativecommons.org/licenses/by-nc-nd/3.0/).

1. Introduction

In marine systems, lithogenic particles are refractory assemblages of crustally-derived minerals that transit the water column largely unaltered. Lithogenics are one of three overarching classes of particles present in marine systems, together with *biogenic particles* (living and dead organic matter and mineral skeletons) and other abiotically-derived *authigenic particles* produced and cycled in situ (e.g. Fe and Mn oxides, barite). Lithogenics, as a major class of particulate matter, are typically not a dominant component of marine vertical particle fluxes in much of the open ocean (Francois et al., 2002) far away from lithogenic inputs such as eolian dust and lateral transport of continental margin sediments. The subtropical North Atlantic, however, is heavily influenced by mineral dust deposition (Mahowald et al., 2005): lithogenics account for between 40% and 72% of the vertical sediment trap flux at productive margin systems between the Cape Verde Islands (CVI) and Cape Verde, Senegal (Ratmeyer et al., 1999), compared to typically less than 20%, and frequently less

than 5%, at open ocean stations distant from eolian dust sources (Francois et al., 2002). The North Atlantic, where 43% of annual dust deposition is estimated to occur (Jickells et al., 2005), thus provides an opportunity to examine lithogenic particle distributions and behaviors in a basin dominated by lithogenic inputs.

Each year, large quantities—1 Pg (Ginoux et al., 2004; Mahowald et al., 2009)—of crustally-derived particles cycle through the world oceans. Although most of this material settles or sinks through the water column unchanged, it participates in the biogeochemical cycling of many trace elements by acting as a source of dissolved trace elements from dissolution, a scavenging surface for trace metals, and a ballasting agent for marine aggregates. Long-range eolian and subsurface lateral (Moore and Braucher, 2008; Lam and Bishop, 2008) inputs of lithogenics are of special importance due to their ability to deliver bio-limiting micronutrients directly to productive surface ocean ecosystems.

In this paper we present, examine, and model the first basin-wide, full-depth zonal transect of marine lithogenic material. We differentiate this material from other particulate analytes through principal component analysis (PCA) of a large multi-element dataset, then examine three elements—Al, Fe, and Ti—that act predominantly as tracers of lithogenic particles. Concentration distributions of these three elements provide information about eolian, lateral/margin, bottom resuspension, and hydrothermal

* Corresponding author at: MIT-WHOI Joint Program in Oceanography, Massachusetts Institute of Technology/Woods Hole Oceanographic Institution, Woods Hole, MA 02543, USA.
E-mail address: dan@whoi.edu (D.C. Ohnemus).

inputs, which are major controls on the basin's total metal fluxes. Elemental ratios provide further insight into element-specific alteration processes and site-specific inputs.

The refractory nature of particulate Ti and its dust-dominated input to the surface of the subtropical gyre presents an opportunity to model vertical particle distributions and underlying dynamic processes using a passive tracer. We present a 1-D model that qualitatively describes the distributions of refractory particulate metals in marine systems, and perform sensitivity tests on how variations in aggregation, disaggregation, and sinking rates may affect size-fractionated field data.

2. Methods

2.1. Study region

Particulate samples were collected at 22 stations across the subtropical N. Atlantic during US GEOTRACES North Atlantic Zonal Transect cruises KN199-04 and KN204-01 aboard the R/V *Knorr* (Fig. 1). Cruise KN199-04 in October 2010 occupied stations 10-01 through 10-12 in the eastern basin, including key stations (Fig. 1, annotations) 10-01 near Lisbon and within influence of the Mediterranean outflow, 10-09 located 200 km west of the Mauritanian shelf break, and 10-12 at the Cape Verde Ocean Observatory (CVOO, formerly known as TENATSO) time series site 70 km NE of the Cape Verde Islands. Cruise KN204-01 in October–November 2011 occupied stations 11-01 through 11-24 from Woods Hole to Cape Verde, including seven in situ pumping stations along Line W between Woods Hole and Bermuda at the BATS site (stn. 11-10); stn. 11-16 at the TAG hydrothermal site along the mid-Atlantic ridge (TAG/MAR); and a KN204/KN199 crossover station at the CVOO site.

The meridional component of the cruise (stations 10-01 to 10-09) is characterized by North Atlantic Central Water (i.e., relatively warm and salty waters between 20–30 °W and 30–35 °N that characterize the North Atlantic subtropical thermocline) in the upper 500 m, high salinity Mediterranean Outflow Waters between 500 and 1500 m, and North Atlantic Deep Water with some Antarctic Bottom Water below that (Jenkins et al., 2015). The zonal portion of the transect can be separated into three sections. From west to east, these are: the Line W section between Woods Hole, MA and Bermuda (stations 11-01 to 11-10), the oligotrophic open ocean section between Bermuda and Cape Verde Islands (stations 11-10 to 11-24), and the Mauritanian Upwelling section between Cape Verde and the Mauritanian coast (stations 10-12 to

10-09). North Atlantic Central Water dominates the thermocline (upper ≈ 600 m) in the Line W and oligotrophic sections, whereas Atlantic Equatorial Water (i.e., fresher and cooler thermocline waters at 20–40 °W, 5–10 °N) is more important in the thermocline of the Mauritanian Upwelling part of the section (Jenkins et al., 2015). Northern sourced Upper and Central Labrador Seawater are the dominant intermediate water masses along Line W, whereas southern sourced Antarctic Intermediate Water and Upper Circumpolar Deep Water dominate in the Mauritanian upwelling section, with a mixture of northern and southern sourced intermediate waters in the oligotrophic section. A similar pattern of more northern sourced waters in the west and more southern sourced waters in the east characterizes the deep waters of the zonal section (Jenkins et al., 2015).

2.2. Particle sampling

The dataset described herein comprises 17 elements (Ag, Al, Ba, Cd, Co, Cu, Fe, Mn, Nd, Ni, P, Pb, Th, Ti, V, Y, Zn) and two particulate size classes (0.8–51 μm, and > 51 μm), though we focus here on the predominantly lithogenic tracers Al, Fe, and Ti. Particles were collected via in situ battery-powered pumps (McLane WRT-LV), in a modified dual-flow configuration described in (Cutter et al., 2010; Lam and Morris, 2013).

Twenty-two stations were sampled, typically at sixteen-point depth resolution over two casts within ca. 24 h: a shallow cast during which eight depths were sampled in the upper 1000 m, including four depths in the upper 200 m, and a deep cast during which eight pumps were sampled between 1000 m and the ocean floor. During the 2011 cruise, a 12 kHz pinger at the bottom of the hydrowire allowed closer sampling of near-bottom depths and benthic nepheloid layers when conditions permitted. Pumps were deployed on a trace-metal hydrowire (Hytrel-jacketed Vectran) and operated for four hours at initially programmed pumping speeds of 8 L/min. Each pump was configured with two parallel flowpaths ("QMA" and "Supor") each of which filtered first through a 51 μm polyester pre-filter (hereafter the "large size fraction" or LSF: particles > 51 μm), and then through either paired 0.8 μm polyethersulfone Supor™ filters (hereafter: "small size fraction" or SSF: particles 0.8–51 μm), or paired quartz fiber Whatman QMA filters (not discussed here). Both QMA and Supor flowpaths were independently flow-metered to determine volume filtered. Combined flowpath outflow was metered separately to ensure volume determination in the event of a single flowmeter failure. Typical total volumes filtered were 1500–1700 L, with 30% of volume (median: 461 L) passing via the Supor flowpath and the rest (median: 1167 L)
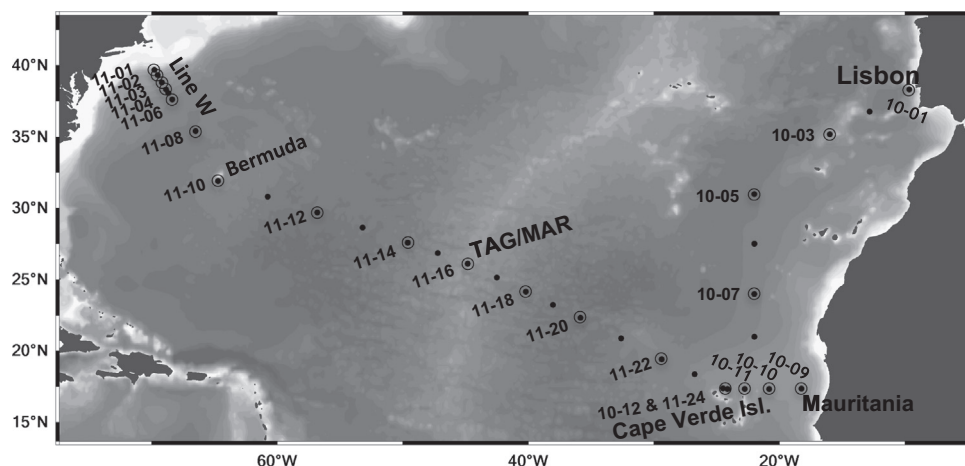

Fig. 1. Oceanographic stations from *R/V Knorr* cruises KN199-4 in October 2010 (stations 10-xx) and KN204-1 in November-December 2011 (stations 11-xx) where particulate samples were collected (circles and annotations). TAG is the TAG hydrothermal site along the mid-Atlantic Ridge (MAR).

passing via the QMA flowpath. Filters and pre-filters were 142 mm in diameter (126 mm active diameter), acid-cleaned prior to use as detailed in (Cutter et al., 2010), and manipulated in HEPA-filtered clean environments using trace-metal clean techniques.

Immediately after pump recovery, particles on one-eighth wedge subsamples of the QMA-side pre-filters (LSF, mean: 145.9 L seawater equivalent) were rinsed from the polyester pre-filter onto acid-cleaned 25 mm, 0.8 μm Supor™ disc filters using 0.2 μm-filtered surface seawater from a contamination-free, towed underway system (Bruland et al., 2005). Primary Supor (SSF) pump filters and the rinse-transferred LSF filters were dried at room temperature in a laminar flow bench and then stored in trace-metal/particle-free cleanroom polyethylene bags. Back in the land-based laboratory, a 1/16 wedge of the *top* Supor filter (representing the 0.8–51 μm SSF; mean: 28.9 L seawater equivalent) was excised using a ceramic rotary blade (Cadence Inc.).

2.3. Analytical techniques

SSF wedges and LSF discs were digested completely using the "piranha" procedure outlined in (Ohnemus et al., 2015). Briefly, filters were first digested using a sulfuric acid and peroxide mixture (piranha reagent) at high heat to digest particulate organic material and the Supor filter matrix. Remaining refractory material was digested using a HCl/HNO$_3$/HF (4 N each) acid mixture at 135 °C for 4 h. All digests were conducted in Teflon vials (Savillex). Final digest material was resuspended in 5% nitric acid for analysis via ICP-MS (Element 2, Thermo Scientific) at the WHOI Plasma Facility, Woods Hole, MA. Elemental recoveries for several certified reference materials (CRMs) using this procedure are presented and discussed in depth in Ohnemus et al. (2015) and were generally > 89%. Average CRM recoveries for PACS-2 and MESS-3 were $94 \pm 9\%$ for Al, $95 \pm 7\%$ for Fe, and $93 \pm 6\%$ for Ti. Indium (10 ppb) was utilized as an internal drift monitor and for matrix/salt suppression correction (typically < 10%). Concentrations were standardized to external dilutions of a combined trace metal standard prepared from ICP/AA standards in 5% nitric acid.

2.4. Synchrotron X-ray methods

Synchrotron x-ray images of intact, dried LSF aggregates still on the polyester pre-filters and extended micro-focused x-ray absorption near-edge spectroscopy (μXANES) of Ti-rich and Fe-rich particles in the SSF were collected at beamline 10.3.2 at the Advanced Light Source, Berkeley CA. X-ray methodology is described further in the Supplemental materials.

2.5. A note on units and plotting conventions

Measurements of particulate metal concentrations in this paper are reported in molar units (nanomoles per liter of seawater filtered), with metal ratios expressed as mole ratios. In some cases, primarily when discussing relationships to crustal material, units of mass or mass ratios will be expressly mentioned.

In section plots plotted in Ocean Data View (ODV; Schlitzer, 2013), the x-axis scales are different for the Line W transect (stns. 11-01 to 11-08), the zonal transect (stns. 11-10 to 11-22, and 10-12 to 10-09), and the meridional section from Mauritania to Lisbon (stns. 10-07 to 10-01) to better display features in regions of strong gradients. A 300 km distance padding was added between the cruise-overlap stations at Cape Verde (stns. 10-12 and 11-24) to allow data from both occupations to be shown. Actual spatial relationships between stations are shown in map views (Figs. 1 and 10). Minimal gridding/interpolation is used to allow visualization of the strong particle gradients observed.

3. Results

3.1. Dataset at a glance: correlations and PCA

Our full dataset contains 17 elements from small size fraction (SSF, 0.8–51 μm) and large size fraction (LSF, > 51 μm) particles in 344 samples from 22 stations. For bivariate correlations, we concentrated on water column associations and excluded samples associated with benthic nepheloid layers (BNLs) and hydrothermal systems by restricting analysis to samples with pFe < 7 nmol/L, leaving 309 of 344 samples (Table 1).

Within the SSF, Fe, Ti, ^{232}Th, Nd, V, and Y demonstrated the strongest positive correlations with Al ($R \geq 0.84$), a typical lithogenic element (Table 1A). These lithogenic relationships hold across many orders of magnitude (Fig. 2), indicating the pervasiveness of lithogenic material throughout the entire basin including the deep interior. Several deviations from dominant correlations (Fig. 2, annotations) indicate element-specific particle inputs and alteration processes further described in the discussion.

Negative correlations between the biomass indicator particulate P and lithogenic elements in the SSF (Table 1A, P) reflect upper ocean maxima of biological production that are coincident with minima of lithogenic particles. We show in the modeling section of our discussion that processes driving these observations are linked through near-surface biotic aggregation and sinking of large particles.

Within the LSF (Table 1B), we observe similarly strong bivariate relationships among Al, Fe, Ti and ^{232}Th. Strong biogenic/authigenic relationships among particulate P, Co, Cd, and Mn are also observed in the LSF, often more strongly than in the SSF. The relative abundance of particulate organic matter is significantly lower overall in the SSF compared to the LSF (Lam et al., 2015), leading to weaker SSF biogenic relationships in that size fraction.

Principal component analysis (PCA) was conducted on a subset of the dataset for which full elemental data were available (199 of 344 samples; 13 elements). Excluded from PCA were the elements Ag, Nd, Ni, and Zn—which were not analyzed at all stations or which had many samples below detection—along with highest abundance samples (pFe > 7 nmol/L) as for bivariate correlations in Table 1. PCA was conducted, in part, using the "PLS Toolbox" for MATLAB developed by Eigenvector Research, Inc., and all elements were first mean-centered and normalized to their standard deviations.

Five principal components can explain 91.3% of total dataset variance for the thirteen elements (Fig. 3). The first component (50% of total variance) is strongly indicative of lithogenic material, as it describes > 85% of the variances for lithogenic tracers Al, Fe, Ti and ^{232}Th. This component also explains > 80% of variances for V and Y, and > 60% for Pb, highlighting that these particulate elements have significant lithogenic components. The second principal component (18.0% of total variance) describes what is primarily biogenic particle variability associated with P, Co, Cd, and Mn distributions. The third component largely describes Ba and Cd, which share subsurface maxima beneath high productivity margin stations. Further components typically describe remaining variance that is largely element specific: the fourth mostly describes particulate Cu variance, highlighting the unique nature of this element; the fifth describes Mn and Pb variances, which have been previously implicated in co-transport via Mn-oxides (Boyle et al., 2005; Sherrell and Boyle, 1992). The remainder of this manuscript focuses on the lithogenic elements Al, Fe, and Ti, indicated by their strong bivariate correlations and grouping in PCA.

3.2. General oceanic distribution of lithogenic particles

Concentration sections of Al, Fe, and Ti are presented in Fig. 4 for the SSF. Considering the strong bivariate correlations previously

Table 1
Bivariate elemental correlation coefficients, R, for the (A) SSF and (B) LSF within a large subset of the data. Dataset has been filtered to remove highly loaded samples present at BNLs, continental margins, and the TAG site by selecting for pFe < 7 nM, leaving 309 (SSF) and 308 (LSF) of 344 samples. Only significant correlation coefficients are shown ($p < 0.05$, by t-test). Bold: positive correlations where $R \geq 0.7$. Bottom rows: strongest three positive correlations for the element listed in that column.

	Ag	Al	Ba	Cd	Co	Cu	Fe	Mn	Nd	Ni	P	Pb	Th	Ti	V	Y	Zn
A: SSF Ag																	
Al																	
Ba		0.34															
Cd			0.48														
Co	0.15	0.18		0.37													
Cu																	
Fe	**0.97**	0.34			0.14	0.13											
Mn	0.30	0.35		0.26	0.58		0.32										
Nd	**0.93**	0.26	0.35		0.39		**0.90**	0.53									
Ni	0.15	0.68	0.33	0.29	0.49	0.12	0.64	0.51	0.61								
P		−0.26	−0.19	0.50	**0.72**		−0.28	0.38									
Pb		0.68	0.26		0.29		**0.72**	0.58	**0.80**	0.55							
Th	**0.95**	0.36					**0.94**	0.28	**0.94**	0.52	−0.28	0.63					
Ti	**0.95**	0.34	0.13		0.18		**0.94**	0.26	**0.90**	0.63	−0.25		**0.93**				
V	**0.86**	0.29	0.17		0.20	0.19	**0.91**	0.44	**0.85**	0.61		**0.76**	**0.85**	**0.82**			
Y	**0.84**	0.38	0.21		0.30		**0.83**	0.47	**0.94**	0.58		0.68	**0.84**	**0.82**	**0.80**		
Zn		−0.34								−0.23	0.21			−0.21			
Max to	Mn Co Ni	Fe Th Ti	Cd Y Th	P Ba Co	P Mn Ni	V Fe Ni	Al Th Ti	Pb Co Nd	Th Y Al	Al Fe Ti	Co Cd Mn	Nd V Fe	Al Fe Nd	Al Fe Th	Fe Al Th	Nd Al Th	P Co Ag
B: LSF Ag																	
Al	0.39																
Ba	0.49	0.21															
Cd	0.55		0.51														
Co	0.52	**0.83**	0.40	0.30													
Cu	0.27				0.30												
Fe	0.41	**0.97**	0.20		**0.84**	0.21											
Mn	0.57	0.50	0.55	0.38	**0.74**		0.47										
Nd	0.40	**0.95**	0.26	0.17	**0.88**		**0.95**	0.63									
Ni	0.43	**0.79**	0.30	0.18	**0.76**	0.14	**0.83**	0.48	**0.85**								
P	0.54	0.19	0.59	**0.86**	0.40		0.15	0.53	0.23	0.26							
Pb	0.19	0.17	0.42		0.20		0.15	0.18	0.17	0.14	0.15						
Th	0.35	**0.97**	0.20		**0.82**		**0.96**	0.50	**0.99**	**0.75**	0.15	0.15					
Ti	0.34	**0.93**	0.18		**0.77**		**0.94**	0.40	**0.95**	**0.74**		0.13	**0.94**				
V	0.46	0.55	0.51	0.43	0.62	0.12	0.53	0.59	0.55	0.54	0.62	0.11	0.52	0.49			
Y	0.33	**0.81**	0.23	0.15	**0.73**		**0.80**		**0.83**	0.65	0.21	0.15	**0.82**	**0.79**	0.49		
Zn		0.18			0.17	0.19	0.16				0.15				0.14		
Max to	Mn Cd P	Fe Th Nd	P Mn V	P Ag Ba	Nd Fe Al	Co Ag Fe	Al Th Nd	Co Nd V	Th Al Fe	Nd Fe Al	Cd V Ba	Ba Co Ag	Nd Al Fe	Nd Th Fe	Co P Mn	Nd Th Al	Cu Ba Co
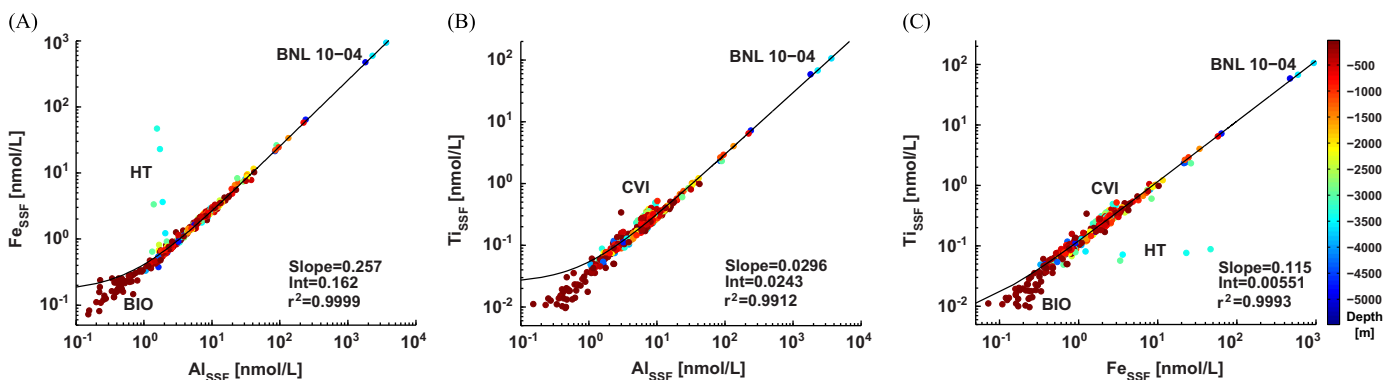
Fig. 2. Concentration scatterplots showing SSF elemental ratios of (A) Fe:Al, (B) Ti:Al, (C) Ti:Fe on log–log scales for the entire N. Atlantic dataset, demonstrating strong correlations observed between lithogenic elements across many orders of magnitude. Linear regressions (black curve) and fit statistics are also shown. Color scale indicates sample depth. Annotations: key regional inputs and notable alteration processes (not all shown in all figures). HT: hydrothermal. CVI: Cape Verde Islands. BNL: benthic nepheloid layer, with station number. BIO: biotic uptake. AfDust: African dust. SCAV: scavenging. MED: Mediterranean outflow. LSW: Labrador seawater. NAm: North American boundary particulates. (For interpretation of the references to color in this figure legend, the reader is referred to the web version of this article.)

described, views illustrated by these sections are unsurprisingly similar, though several inputs and processes are more notable in specific elements. Highest lithogenic concentrations by several orders of magnitude (Fig. 4, caption) are observed in BNLs,

especially at the western margin. Lowest lithogenic concentrations are generally observed in the upper 200 m at nearly all stations, with minima at the deep chlorophyll max (DCM) that are especially pronounced in the subtropical gyre (stns. 11-12 to 11-22 and 10-05;

Variance Captured for a 5 PC Model
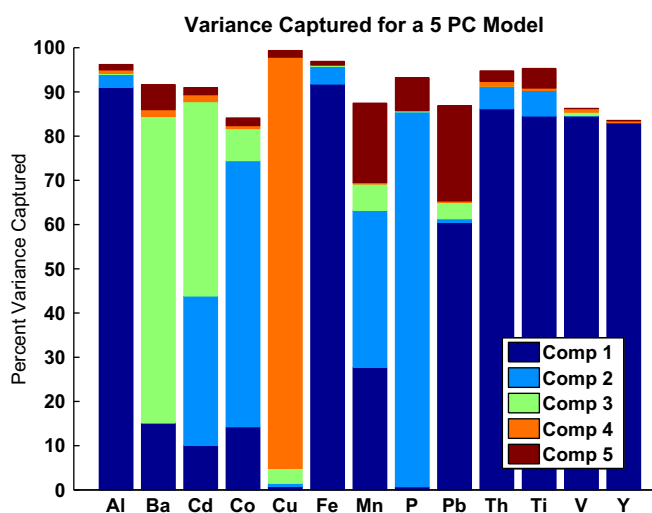
Fig. 3. Variance of thirteen particulate elements captured by the first five principal components in principal component analysis. Component 1 captures 50.0% of total dataset variance and most lithogenic elemental variances; Comp 2: 18.0%; Comp 3: 10.4%; Comp 4: 7.8%; Comp 5: 5.2%.

< 600 pM Fe$_{SSF}$). These low surface concentrations—and the frequent absence of any mixed layer lithogenic maximum that would normally be considered evidence for eolian/dust inputs—are, we will show, not in conflict with general understanding of the North Atlantic as strongly influenced by eolian deposition, as also proposed by Dammshäuser et al. (2013).

Mid-water column (500–3000 m) lithogenic concentrations are elevated nearer the continental margins compared to open ocean loads. High lithogenic loads are observed between Cape Verde and Mauritania beneath the Saharan dust plume (stns. 10-09 to 10-12; and 11-24), and near Lisbon (stn. 10-01) within influence of the Mediterranean outflow. High lithogenics are also found along oceanographic Line W from Cape Cod to Bermuda (stns. 11-01 to 11-10) associated with boundary current/shelf interactions along the North American continent. Hydrothermal inputs near the mid-Atlantic ridge system (MAR) are evident in Fe concentration sections via high particulate Fe loads within the neutrally-buoyant hydrothermal plume sampled near the TAG vent site (stn. 11-16; up to 46 nM pFe at 3300 m).

Size partitioning between the SSF and LSF is very similar for the three tracers, shown for Fe in Fig. 5. In the upper ocean between the mixed layer and 200 m, lithogenics partition strongly (50–80%) to the LSF. This partitioning decreases to 25–40% between 200–500 m depth, and below 500 m, with few exceptions, lithogenics are predominantly found in the SSF (80–95%). Micro x-ray fluorescence (μXRF) images (Fig. 6) of LSF aggregates from a range of depths at stn. 10-09 near the Mauritanian coast visually demonstrate that LSF lithogenics, even near African dust sources, are not intrinsically large (> 51 μm), but are mostly micron-sized eolian particles packaged into LSF aggregates.

4. Discussion

4.1. Lithogenic ratios

4.1.1. Bulk input composition and processes

Strong correlations between lithogenic elements in size-fractionated particles (Table 1 and Fig. 2) and a strong apportionment in PCA (Fig. 3) that includes several other elements, indicate a central role for lithogenic particles in controlling North Atlantic

metal distributions. Concentration sections of lithogenic tracers (Fig. 4) demonstrate the similarities in bulk lithogenic inputs, while ratio sections of the tracers (Fig. 7) highlight naturally occurring lithogenic input variations. Notably, when marine lithogenic ratios are compared to various crustal (BCC: bulk continental crust; UCC: upper continental crust) and eolian dust (AD: African dust) input ratios, no single source can fully explain all three sections. This indicates both variation in lithogenic inputs across the basin and internal biogeochemical processes such as abiotic scavenging, dissolution, and biotic uptake that modify elemental ratios.

Of the three elements, Ti and Fe vary more as a function of source than Al (Ti: 0.54 wt% BCC, 0.3% UCC versus Al: 8.4% BCC, 8.0% UCC and Fe: 7.1% BCC, 3.5% UCC; Taylor and McLennan, 1995). Since Ti is not a known micronutrient and thus not subject to biological uptake like Fe, broad basin-scale variations of the SSF Ti:Al section are thus good indicators of lithogenic source (Fig. 7c). Open ocean stations between Bermuda and Cape Verde exhibit ratios reflective of African dust inputs (Ti:Al 0.037–0.045 vs. "AfDust" ratio 0.047), while stations near the North American margin ("NAm") possess generally lower, BCC-like ratios (Ti:Al 0.028–0.040 vs. BCC$_R$ 0.036). Kuss and Kremling (1999a) reported similar Ti:Al ratios in a sediment trap located at 33°N,21°W, NW of the Canary Islands and near 10-05 (0.036). Source variability is also notable near the Cape Verde Islands (Fig. 7, "CVI") where enrichment of Ti in basaltic mineral phases sourced from proximal ocean island sources (Rothe, 1973; Plewa et al., 2012) affects the Ti ratios of local particles. Mineralogy of these particles is examined in Section 4.3.

Ratios of Ti and Al have been used as sedimentary tracers for aluminosilicate accumulation rates over glacial time scales (Boyle, 1983), to differentiate fluvial vs. eolian inputs (Zabel et al., 1999), and to distinguish inputs based on grain-size, especially on the continental margin (Stuut, 2005; Bloemsma et al., 2012). Here, variations in Ti:Al ratios in water column lithogenic particles indicate differences in lithogenic source from North America, African Dust, or Cape Verde Islands (Fig. 7).

Particulate Al:Fe ratios (Fig. 7a,d) demonstrate an apparent near-boundary and depth-dependent scavenging enrichment ("SCAV") for Al, especially in the SSF, which we explore further in Section 4.5. Enrichment of Al is also observed in Mediterranean-outflow particles ("MED"), benthic nepheloid layers ("BNL") along the western boundary, and in the upper 500 m along Line W perhaps in association with detached/intermediate shelf nepheloid layers. Elevated Al:Fe ratios in the western portion of the section may reflect boundary current-associated resuspension of N. American crustal material (Lisitzin, 1972; Moran and Moore, 1991) with an elevated Al content ("UCC$_T$").

Particulate Fe:Ti ratios are elevated in the SSF in surface waters, and less so in the LSF, consistent with active biotic accumulation and recycling of Fe by small organisms ("BIO"). The TAG hydrothermal vent is a source of particulate iron, present as fine Fe-oxyhydroxides (German and von Damm, 2006), to the ocean interior. The influence of this and other hydrothermal systems ("HT") along the mid-Atlantic ridge can be seen in mid-water particulate ratios hundreds of kilometers away from the ridge axis, especially to the west. Samples with elevated Fe:Ti from both surface waters and the hydrothermal plume were observed to have a higher fraction of oxalate-leachable labile iron (Revels et al., 2015), suggesting that elevated Fe:Ti ratios are indicators of more labile particulate Fe.

The Mauritanian OMZ sampled between stns. 10-09 and 10-12 is characterized by elevated dissolved Fe (e.g. Noble et al., 2012; Fitzsimmons et al. 2013). Here, this elevated dissolved Fe is predominantly present as complexed Fe(III) (Croot and Heller, 2012), and the lack of changes in particulate Fe:Ti ratios within or at the OMZ boundaries (Figs. 7b,e) suggests no enhanced scavenging onto nor dissolution of Fe from local particles. Scavenging or other biogeochemical signals in this basin may, in general, be a
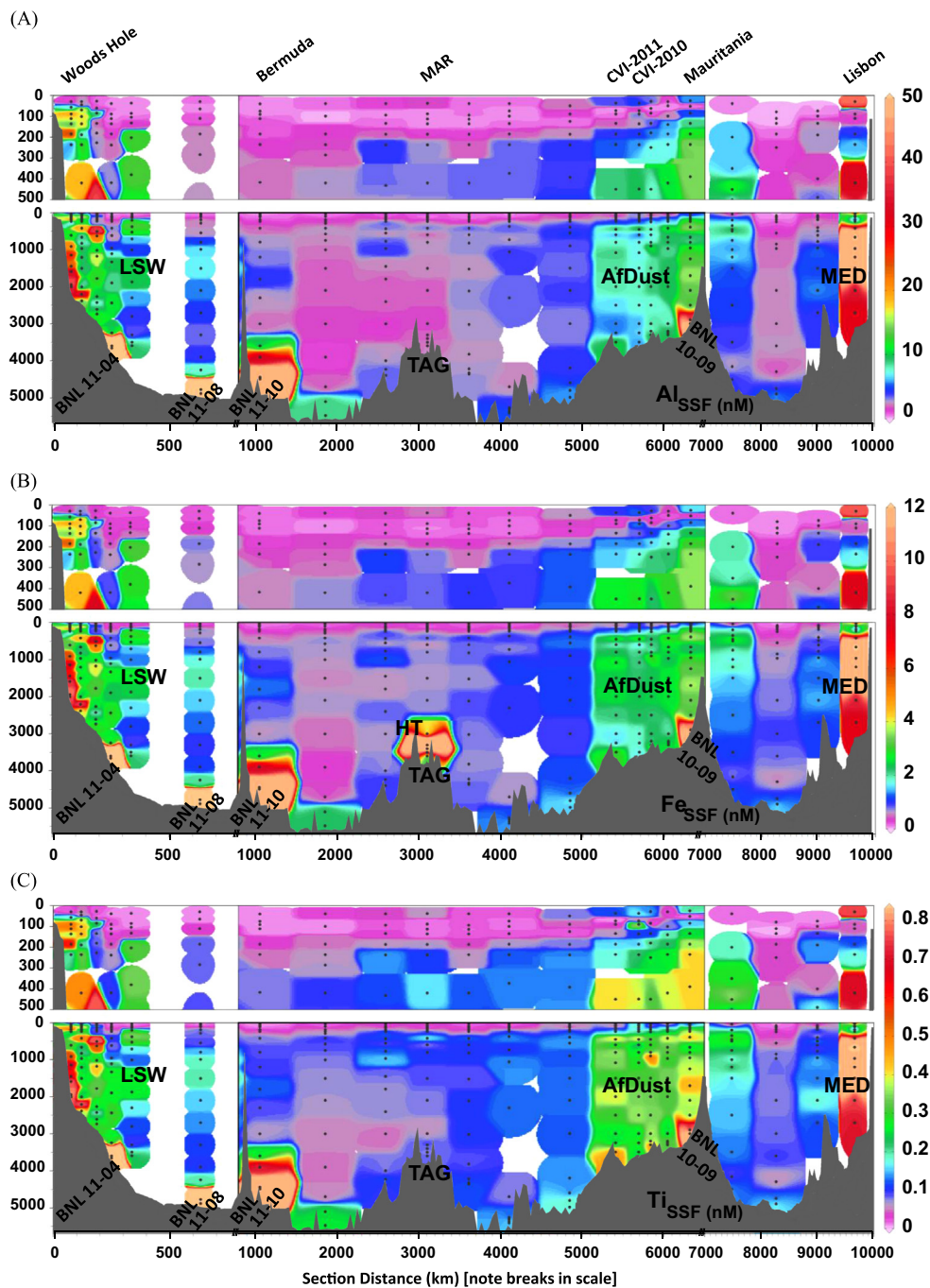
Fig. 4. Concentration sections of (A) Al_{SSF}, (B) Fe_{SSF} and (C) Ti_{SSF} in units of nmol/L. *X*-axes: section distance (km) including breaks (double bars) to consolidate views; note changes in scale between breaks. *Y*-axes: depth in meters. Figure annotations: notable lithogenic inputs and processes as described in Fig. 2. Concentrations in excess of plotted ranges include BNL 11-04 (Al: 3.6 μM, Fe: 938 nM, Ti: 106 nM), BNL 11-08 (Al: 1.81 μM, Fe: 470 nM, Ti: 58 nM), BNL 11-10 (Al: 84.8 nM; Fe: 21.4 nM; Ti: 2.3 nM), TAG (Fe: 46.6 nM), BNL 10-09 (Fe: 26.3 nM), MED (10-01, 665 m, Al: 222 nM; Fe: 57.6 nM; Ti: 6.47 nM).

small signal relative to the highly elevated lithogenic particle fluxes, a point also noted in trap data by Kuss and Kremling (1999a).

Biogeochemical processes such as dissolution, scavenging, and biotic recycling should influence the SSF more strongly due to the higher abundances, longer residence times, and greater scavengable surface area in the SSF compared to the LSF. Of the SSF and LSF ratios examined, Ti:Al ratios were most similar across size fractions (Figs. 7c,f), indirect evidence that Ti is less susceptible to these processes than other lithogenic elements, and consistent with studies of dissolved and particulate Ti and Al (Dammshäuser et al., 2013).

4.1.2. Lithogenic normalization

Which element (Al, Fe, or Ti) is the best choice as a lithogenic normalizer? Biological Fe enrichment in fine surface particles (Fig. 7b) eliminates Fe as a general marine lithogenic normalizer, at least in the upper ocean and in particle regimes where biotic contributions vary significantly in time. Al is a more traditional choice for lithogenic normalization, as it varies minimally between canonical continental sources (UCC: 8.04 wt% vs. BCC 8.41 wt%; Taylor and McLennan, 1995). Previously described scavenging of dissolved Al onto particles near ocean margins and/or with increasing depth could, however, lead to overestimation of the lithogenic fraction.
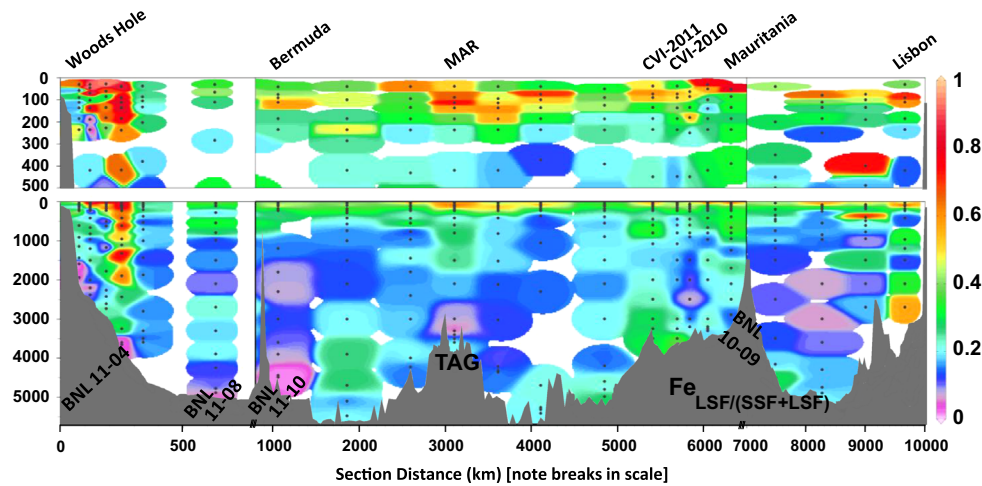
Fig. 5. Typical lithogenic particulate size-fractionation, shown here for Fe, as $Fe_{LSF}/Fe_{(SSF+LSF)}$. Lithogenic material partitions strongly into the LSF in the upper 200 m at most stations, with SSF abundances dominating in the sub-euphotic ocean interior.
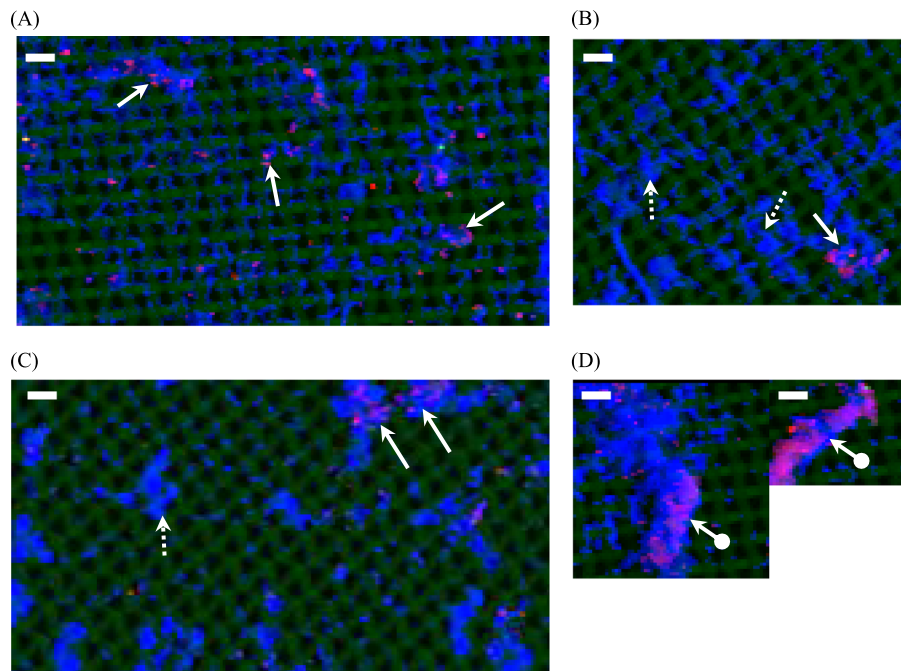
Fig. 6. Tricolor μXRF maps of > 51 μm LSF marine aggregates on polyester prefilters, from four depths at the station closest to Mauritania (stn. 10-09). Blue: particulate Cl (sea-salt) preferentially retained in aggregates as samples dry, allowing visualization of aggregate shapes. Green: Ti, showing the underlying 51 μm prefilter grid. Red: particulate Fe, showing aggregates retaining fine (< 51 μm) dust particles (solid arrows) compared to aggregates without dust (dashed arrows). Some aggregates contain large amounts of fine dust (bulbed solid arrows), leading to clumped appearances. (A) mixed layer (ML, 23 m); (B) deep chlorophyll max (DCM, 52 m); (C) oxygen minimum zone (OMZ, 390 m); D): deep interior (1700 m). Scale bars (white): 100 μm. (For interpretation of the references to color in this figure legend, the reader is referred to the web version of this article.)

Titanium concentrations vary much more as a function of crustal source than Al, but have the advantage of not being as affected by significant scavenging from dissolved pools (cf. Al) (Dammshäuser et al., 2013) or biological uptake and recycling (cf. Fe). Titanium's utility as a lithogenic normalizer thus depends on the likelihood of significant variations in the Ti composition of lithogenic sources in time or space.

Titanium may be especially useful for determining excess (non-lithogenic) particulate Fe in marine particles, since the ratio of Fe:Ti remains relatively constant between source regions (Fig. 7b). Throughout the central and eastern basin, Ti-rich African dust-like Fe:Ti and Ti:Al ratios are observed, while Ti-poor particles from N. America are observed more generally in the western basin along Line W (Fig. 7b,c). This type of broad input homogeneity is conducive to meaningful lithogenic determinations. With improved understanding of marine lithogenic metal inputs, source/end-member variations, and in situ scavenging behaviors, we can improve lithogenic corrections conducted using both Al and Ti.

4.2. Benthic nepheloid layers

Benthic nepheloid layers (BNLs) are notable in this dataset for their extremely high lithogenic metal concentrations, similar to previous observations of intense BNLs in the west Atlantic (Brewer et al., 1976; Biscaye and Eittreim, 1977). We observed concentrations of particulate Fe in western-basin nepheloid layers that approached the micromolar level ($pFe_{total} = 973$ nM, stn. 11-04), nearly three orders of magnitude greater than typical mid-water column (1000–3000 m) open ocean pFe concentrations of ≈ 1 nM.
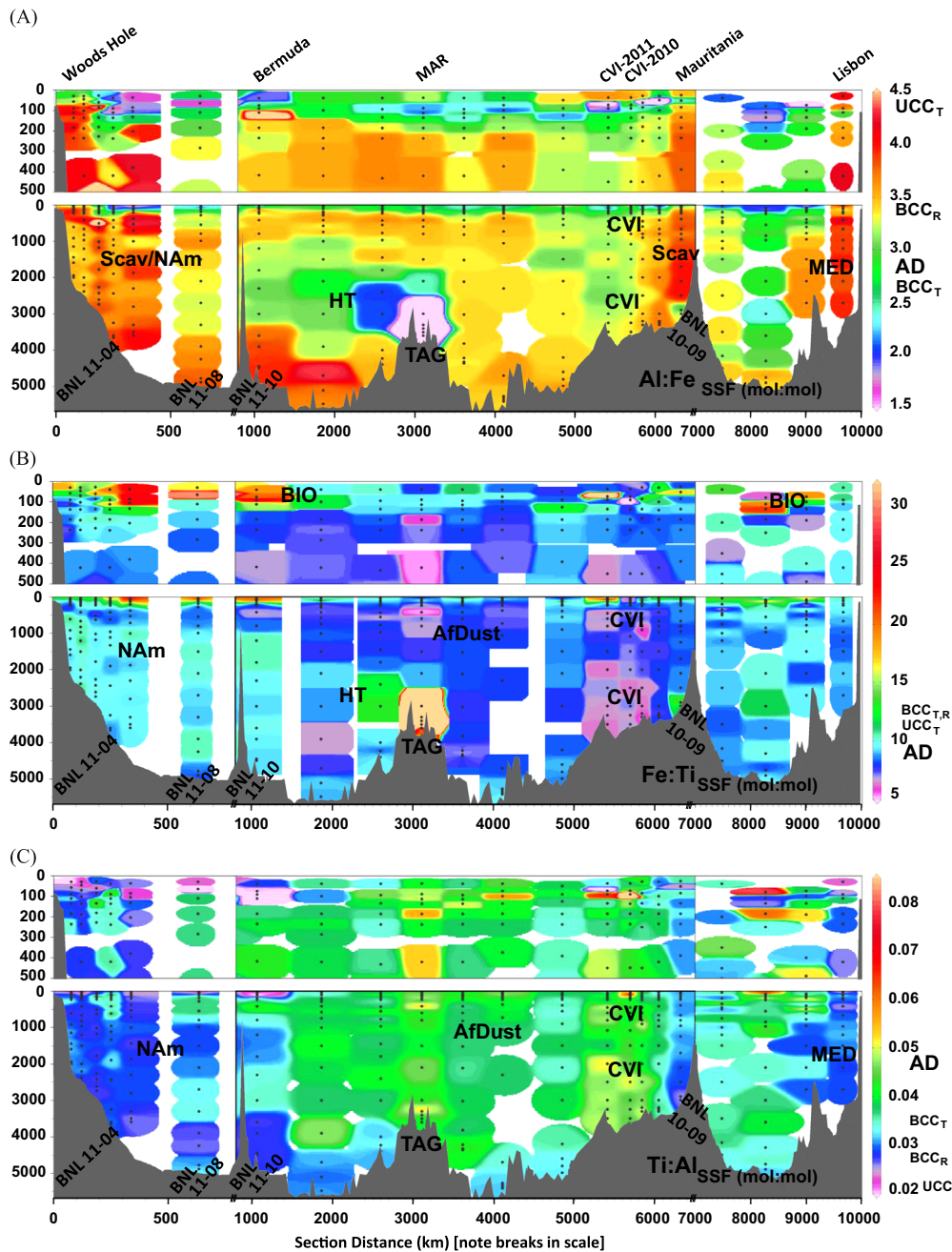
Fig. 7. Mole ratio sections of (A) $Al:Fe_{SSF}$, (B) $Fe:Ti_{SSF}$, (C) $Ti:Al_{SSF}$, (D) $Al:Fe_{LSF}$, (E) $Fe:Ti_{LSF}$, and (F) $Ti:Al_{LSF}$. X-axes: section distance (km), including breaks (double bars) to consolidate views. Y-axes: depth in meters. Figure annotations: notable lithogenic inputs and processes as described in Fig. 2. Scale bar annotations: key crustal ratios including bulk continental crust (BCC) from (BCC$_T$: Taylor and McLennan, 1995) and (BCC$_R$: Rudnick and Gao, 2003), upper continental crust (UCC$_T$: Taylor and McLennan, 1995), and bulk African dust (AD) collected during *KN199* near Mauritania (W. Landing and R. Shelley, pers. comm.).

Key chemical differences were also noted between an African margin BNL sampled near Mauritania (stn. 10-09) and western margin BNLs. Particles from a Mauritanian BNL sampled beneath the intense Saharan dust plume (Mahowald et al., 2009) were strongly enriched in particulate Fe (relative to Ti, Fig. 7b "BNL 10-09") and Mn (not shown). Iron enrichment was especially notable compared to overlying, mid-water column particles, suggesting reductive mobilization of dissolved Fe and Mn in nearby sediments.

Sedimentary-sourced pyrite (Fe-sulfide) has been previously reported in regional waters (Lam et al., 2012), and work on local sediments has suggested through sedimentary particulate metal profiles (Nolting et al., 1999) and elevated porewater Fe^{2+} concentrations (Dale et al., 2014) that reducing sedimentary conditions exist along this margin. A reductive source of Fe also suggested by isotopically light redox-mobilized Fe (Severmann et al., 2010) is reported in particles from this BNL by Revels et al. (2015). Redox-mobilized metals can precipitate within shallower, oxygenated sediments that are later resuspended and transported laterally or downslope as BNLs, as previously described off Mauritania by Fischer et al. (2009). Mobilized metals can also precipitate in the water column itself, after diffusion from porewaters. Both scenarios lead to authigenic mineral/oxide formation that enriches pFe and pMn in suspended particles. The chemical distinction of BNL particles near Mauritania versus those in the western basin could reflect this BNL's location beneath an upwelling system and the associated high productivity (Carr, 2002) and vertical flux (Bory et al., 2001; Ratmeyer et al., 1999; Iversen and
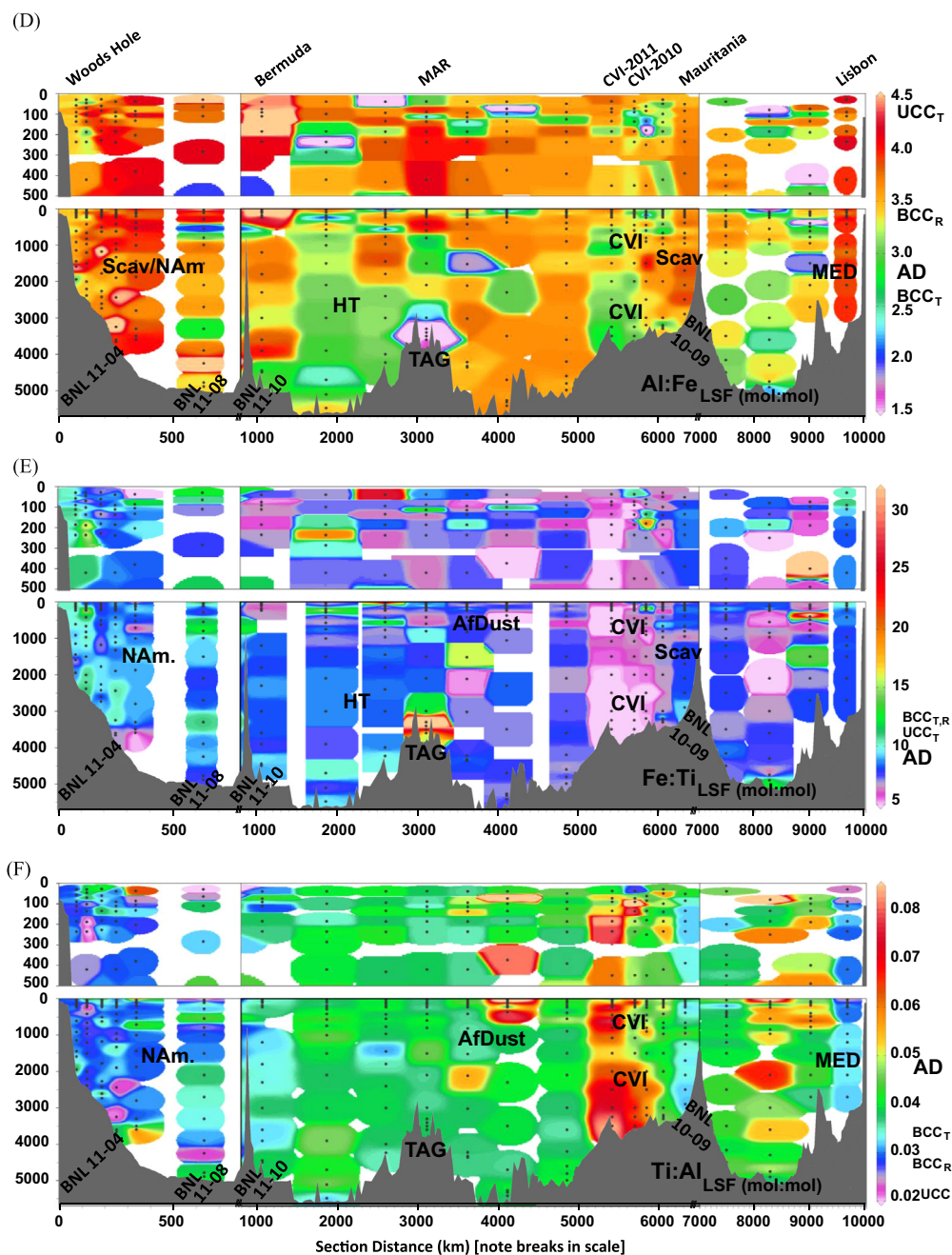
Fig. 7. (*continued*)

of organic carbon, creating benthic conditions amenable to sustained reductive metal mobilization.

Lithogenic ratios in BNLs along the western margin, by comparison (Fig. 7, BNLs 11-04/-08/-10), do not show notable Fe or Mn enrichment compared to overlying particles, and may even be slightly Fe poor (cf. BNL 11-08, Fig. 7b) relative to Ti. Previous observations of Fe excesses in N. Atlantic BNLs (Lambert et al., 1984) were calculated using a fixed Fe:Al mass ratio of 0.60 (Al:Fe mole ratio of 3.4 for comparison to Fig. 7a). Our dataset shows little evidence for systematic Fe excess relative to Al or Ti in western BNLs, especially in comparison to most of the intermediate column (Fig. 7a,b). Lambert et al. observed no Mn excess and only slight Fe enrichment (13%) at GEOSECS stn. 120, their closest reported station to our transect, near our station 11-14. The extremely high lithogenic concentrations observed in western

BNLs may indicate that continued, presumably turbulent, resuspension of large amounts of material necessary to sustain such BNLs, either precludes reductive sedimentary processes entirely or masks authigenic oxide signals via large inputs of crustal-like material.

Most open ocean stations between Bermuda and Cape Verde exhibit near-bottom decreases in the SSF Ti:Al ratio (benthic Ti: Al$_{SSF} \leq 0.035$ vs. overlying ratios ≥ 0.035), regardless of whether a BNL was observed at the time of sampling. These benthic ratios could represent both proximal and distal effects. Proximal effects could include sedimentary release of dAl during diagenesis and in situ Al-scavenging onto local suspended particles, enhanced scavenging of dAl because of higher particle loads in association with nepheloid layers (Rutgers van der Loeff and Boudreau, 1997), or local resuspension of Al-enriched sediments (Murray and

Leinen, 1996). Distal influences potentially include far-field suspended lithogenic signatures associated with deep water masses and any initial and/or acquired signatures of suspended particles or dissolved metals therein (Diekmann et al., 2004; Petschick et al., 1996).

We also note shifts in size-fractionation of benthic particles from ≤ 25% LSF mid-water column to 25–35% LSF up to or exceeding 500 m above bottom (m.a.b) in association with lithogenic maxima at many open ocean eastern basin stations (cf. Figs. 4 and 5, stns. 11-20 through 11-24, 10-05, and 10-07). These stations did not appear to have notable BNLs at the time of sampling. McCave (1983) noted 2- to 3-fold increases in coarse mode particles up to 500 m.a.b. near the Nova Scotia continental rise, even at relatively quiescent stations. He attributed these to mixtures of bottom-resuspended, truly coarse particles (primarily to depths < 250 m.a.b.) and temporal variation in euphotic zone-sourced aggregates (250–500 m.a.b.). In the abyssal stations of our dataset, horizontal inputs of lithogenic particles that are > 51 μm, or enhanced resuspension of LSF relative to SSF particles to 500 m. a.b. seem unlikely. This observation might be explained by enhanced in situ aggregation rates of SSF lithogenic particles into LSF aggregates nearer the ocean bottom, though the underlying mechanisms for this enhancement remain unclear.

4.3. Classification of particulates using Ti-μXANES

Particles collected near the Cape Verde Islands (CVI) were especially high in Ti (Figs. 7c,f; "CVI"), likely indicating the presence of Ti-rich minerals sourced from CVI ocean island basalts (OIB) (Rothe, 1973; Plewa et al., 2012) transported via locally sourced dust and/or sub-surface lateral inputs. The strong distinction in input end-member composition near CVI compared to background lithogenic ratios—Ti:Al ≈ 0.5 by wt. in OIB inputs (Davies et al., 1989; Prytulak and Elliott, 2007) versus 0.07 (Stuut, 2005) or 0.047 (Shelley et al., 2015) in African dust inputs —prompted closer mineralogical assessment. Using Ti K-edge μXANES, we compared the Ti-mineralogy of two marine samples collected near CVI (stn. 10-12: 800 m and 2000 m) to two marine samples and an aerosol sample collected adjacent to Africa/Mauritania (stn. 10-09: 800 m and 2000 m; aerosol sample provided by R. Shelley and W. Landing).

African aerosols and the 800 m sample collected at stn. 10-09 were both primarily mixtures of the Ti-oxides anatase and rutile, with smaller contributions of ilmenite ($FeTiO_3$) and biotite (mica) (Suppl. Fig. 1). The excellent Ti compositional agreement is evidence that dust is a principal source of Ti to the water column. The deeper (2000 m, stn 10-09) African marine sample, potentially more influenced by lateral slope and margin sediments (Revels et al., 2015), lacked the ilmenite and mica components found in the aerosol and the 800 m marine sample; instead, this deeper sample displayed a relative increase in rutile. This apparent phase-replacement by oxides may indicate that water column or sedimentary diagenetic processing of Ti-minerals has occurred, as Fe^{2+} present in ilmenite can be diagenetically removed to leave behind a rutile matrix (Morad and Aldahan, 1986). A separate lateral source of rutile-rich lithogenic material to this depth, perhaps from margin/slope sediments is also a possibility.

Cape Verde Islands-influenced marine particles (stn 10-12, 800 and 2000 m) were better described by a mineral spectrum—presumed titanomagnetite due to its strong similarity to published XANES spectra (Suppl. Fig. 1; Pearce et al., 2012), known frequency in local lava flows, and highly variable Ti content (Knudsen et al., 2005)—which exceeded 50% of fits at 800 m and approached 20% at 2000 m. Local Ti:Al ratios and Ti μXANES data point to a mineralogically distinct source of Ti-rich lithogenics from ocean islands, consistent with previous studies (Plewa et al., 2012). Other

ocean island hotspots with modern magma sources known to be variably Ti-rich include Hawaii, Samoa, Iceland, and the Galapagos (Jackson et al., 2008). These point sources of OIBs may similarly alter local suspended Ti particle composition compared to dominant background inputs. Particulate compositional gradients in these regions may thus present oceanographic opportunities for examination of lateral metal input variations and associated vertical particle dynamics.

Large/LSF aggregates near CVI possessed notably higher Ti:Al ratios than fine/SSF particles (Fig. 7c, f) which appears counterintuitive in the case of a Ti-rich lateral (and thus presumably SSF) particle source. Direct inputs of truly coarse (> 51 μm) Ti-rich CVI dust is one possibility (Rognon et al., 1996). As discussed later, locally dominant Ti-rich Cape Verdean dust inputs to the SSF may be rapidly packaged into the LSF and exported, allowing such Ti-rich inputs to be more strongly expressed in the LSF, which derives its signature primarily from the surface. Deep SSF particles with slower settling speeds and longer residence times represent a more dilute mixture of CVI-minerals within a background of primarily African-sourced particles.

4.4. Hydrothermal inputs

Hydrothermal systems, though not traditionally considered lithogenic in nature, are nevertheless a significant source of particulate Fe into the deep basin. Fe-μXANES spectra of an SSF sample from the TAG hydrothermal plume (stn. 11-16, 3300 m) showed only ferrihydrite, with no evidence for Fe-sulfides (Suppl. Fig. 2). Particulate samples were dried and stored at room temperature for ≈ 10 months prior to analysis. Previous work has shown that micron-sized pyrite is stable in particulate samples stored under these conditions (Lam et al., 2012), but stability of nano-scale pyrite (cf., Yücel et al., 2010) in the sample is unknown.

Absolute particulate Fe enrichments were not observed in particles at similar depths at flanking stations 11-14 and 11-18, 500 km to the west and east of the ridge axis, respectively (Fig. 4b). There were enrichments in Fe:Ti and Fe:Al, however, in SSF particles from relevant depths at those and other stations, especially to the west (Fig. 7b) where long-term geostrophic flow of neutrally buoyant plume particles is expected (LaCasce and Speer, 1999). This broad hydrothermal input of particulate metals offers a unique opportunity to explore fine particle sinking rates, metal scavenging rates, and sub-surface packaging behaviors in the deep open ocean. The trace metal signatures of other key hydrothermally sourced elements (e.g. Ag, Cd, V, Zn), remain interesting topics for future synthesis.

4.5. Evidence for Al scavenging

Fine particles near ocean margins exhibited Al:Ti enrichment over open ocean/African dust-dominated ratios (Fig. 8, red points; also Fig. 7a: stns. 10-09, stns. 11-01 to -06). Enrichment of Al is also seen at depth, with 20–30% enrichment typical below 2000 m. These results are consistent with preferential scavenging of Al over Ti (Dammshäuser and Croot, 2012; Dammshäuser et al. 2011). A stronger Al:Ti correlation is found for opal ($R^2 = 0.30$) than for total particle concentrations ($R^2 = 0.10$) (Lam et al., 2015), supporting a relationship between Al scavenging and opal (Murray and Leinen, 1996; Dymond et al., 1997; Middag et al., 2009) even if the mechanistic association is not yet known (Vrieling et al., 1999). Alternatively, elevated Al:Ti may be due to different lithogenic sources with elevated crustal Al:Ti compared to African dust, especially at the North American and Iberian margins. If in situ scavenging is responsible for elevated Al:Ti, however, the use of particulate Al totals for lithogenic normalization could lead to significant overestimation of lithogenic abundances (Kuss and
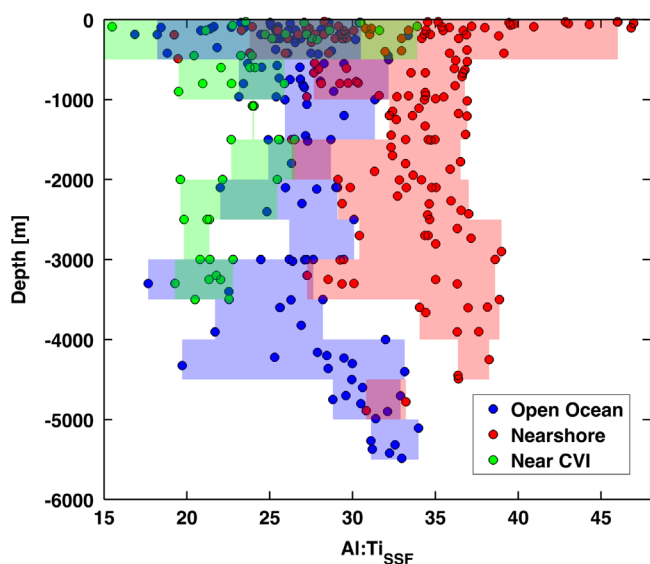
Fig. 8. Fine particles from stations closer to continental margins and at greater depth display elevated Al:Ti mole ratios. Blue: open ocean stations (11-12 to 11-22; 10-05 and 10-07) which generally show Al enrichment primarily with increasing depth. Yellow: stations (10-11, 10-12, and 11-24) with elevated Ti from Cape Verde Islands lithogenic material, which decreases the Al:Ti mole ratio. Red (all remaining stations): nearer-shore stations where Al is found in greater relative abundance on particles throughout the water column. (For interpretation of the references to color in this figure legend, the reader is referred to the web version of this article.)

Kremling, 1999b), especially in deep samples and samples with margin influences, for instance, via Labrador Seawater.

4.6. Eolian and lateral inputs

Terrestrially derived eolian input of mineral dust dominates exogenous lithogenic delivery into the upper water column in the sub-tropical North Atlantic (Jickells et al., 2005; Mahowald et al., 2005). The standing water column inventories of lithogenic particles should thus relate to the basin's dominant eolian deposition patterns if strongly vertical processes (sinking, packaging) control distributions after deposition. Regions where inventories show positive deviation from eolian deposition patterns should indicate lateral sources of lithogenic material from the continental margins, and/or natural variations in vertical processes. We discuss the distribution of eolian and lateral inputs by dividing the section into several depth ranges (0–200 m; 200–1 km; 1–3 km) and examining the station-by-station particulate Ti inventories (Figs. 9a–c) along with bottom-most sample concentrations (Fig. 9d).

Surface lithogenic inventories (Fig. 9a, 0–200 m) are generally very low, displaying rapid decreases away from the N. American margin along Line W and away from the African margin at Mauritania. A slight local surface maximum is observed near Cape Verde ~70 km from the island chain, likely indicating a local or recent dust input. Surface inventories of lithogenic particles reflect recent dust inputs (order: days to weeks) and short-range, margin-sourced lateral inputs as discussed further in section 4.7.

Open-ocean lithogenic inventories in the 200–1 km mid-water column depth range (Fig. 9b), by comparison, consistently increase from west to east along the zonal transect (stns. 11-10 to 11-22). These inventories agree quite well with basin-scale, annual dust deposition patterns estimated by global eolian models (Fig. 9e from Mahowald et al., 2005). Increasing mid-water column inventories between CVI and Mauritania could be consistent with local eolian patterns (Mahowald et al., 2009) or suggest lateral inputs from the African continental margin. Dissolved tracers including ^{228}Ra (half-life 5.75y) suggest little lateral transport at these depths in this region,

however (M. Charette, pers. comm.), implicating a primarily eolian source for lithogenics in the 0–1000 m depth range near Africa.

Elevated near-margin inventories along Line W in both the 0.2–1 km and the 1–3 km depth ranges (Figs. 9b,c) appear unsupported by eolian deposition patterns and indicate lateral sources of lithogenics. A tongue of lithogenics is found in association with Labrador seawater (Fig. 4, "LSW"; Fig. 10c, western margin), a portion of NADW identified by Optimum Multi Parameter Analysis of end member water characteristics (Jenkins et al., 2015) that impinges the continental slope (Bower et al., 2011) and acquires lithogenic particles.

Mediterranean outflow is the other prominent lateral input sampled ("MED" Fig. 4 stn 10-01; Fig. 9c). McCave and Hall (2002) extensively documented Mediterranean water (MW)-associated turbidity using transmissometry, noting the rapidity with which its suspended particulate load is lost as it exits the Gulf of Cadiz and transits along the Portuguese shelf (cf. their Fig. 3). At our station 10-01, located northeast (downstream) of their station M42-02, we observe Mediterranean-sourced fine particles beginning at 420 m depth, with a strong maximum at 695 m (SSF Fe: 57 nM). This MW-associated particulate signal is especially Al-rich (Fig. 7a,d), a signature found at all depths and in both size-fractions beneath the MW plume, indicating both settling of particulate matter out of the MW source and apparent transfer between size-fractions even at depth.

4.7. Lithogenic residence times

Using station-by-station bulk particulate (SSF+LSF) inventories of Ti in several upper ocean depth ranges (Tables 2A B), estimates of the annual average input rates of aerosol dust from the Aeronet_Median deposition model (Table 2C: AEROCOM Phase II, 2013), and assuming a lithogenic dust Ti composition of 0.56% by weight (8% Al by wt., and 0.07 Ti:Al wt. ratio (Stuut, 2005)), we calculate open ocean lithogenic particle residence times (Table 2D) of 6–27d in the upper 200 m, and 48–285 d in the upper 1000 m. Open ocean residence times for lithogenic particles are in good general agreement with those calculated for particulate Ti by Dammshäuser and Croot (2012) (4–37 d, for 0–100 m) in the same region. Note that sub-annual lithogenic residence times indicate that using monthly or rolling-window deposition fluxes derived from measured or modeled sources, rather than annual averages, would improve estimates of residence time.

We also calculate bulk particulate (SSF+LSF) steady state sinking speeds (Table 2E) through each ocean layer by dividing the thickness of the layer by the residence times estimated from dust flux. At the continental margins along Line W and near Lisbon, sinking speeds are skewed by lateral sources of lithogenics at these stations as they were for residence times. In the open ocean, however, an assumption of eolian dust as the only lithogenic input flux is more appropriate. There, two major trends are notable: a general increase in bulk particle speed from west to east, and a general decrease in bulk particle speed as the depth of integration increases.

The main driver of the zonal variations in residence times and bulk sinking speeds is the observation that gradients in Ti inventories (a 2- to 3-fold increase from stn 11-10 to stn. 11-22, depending on the depth of integration) are significantly less than the gradients in estimated annual dust fluxes (a 7-12 fold increase from 11-10 to stn. 11-22; Jickells et al., 2005). Overestimation of dust fluxes in the east or underestimation in the west could account for these trends, but assuming deposition trends are correct, this implies increases in particle removal processes (i.e. greater bulk sinking speeds) beneath regions of greater dust input. Such faster lithogenic removal in the east could be due to additional lithogenic ballasting of sinking particles (Fischer and Karakaş, 2009; Dunne et al., 2007; Ternon et al., 2010; Lima et al., 2013) or differences in
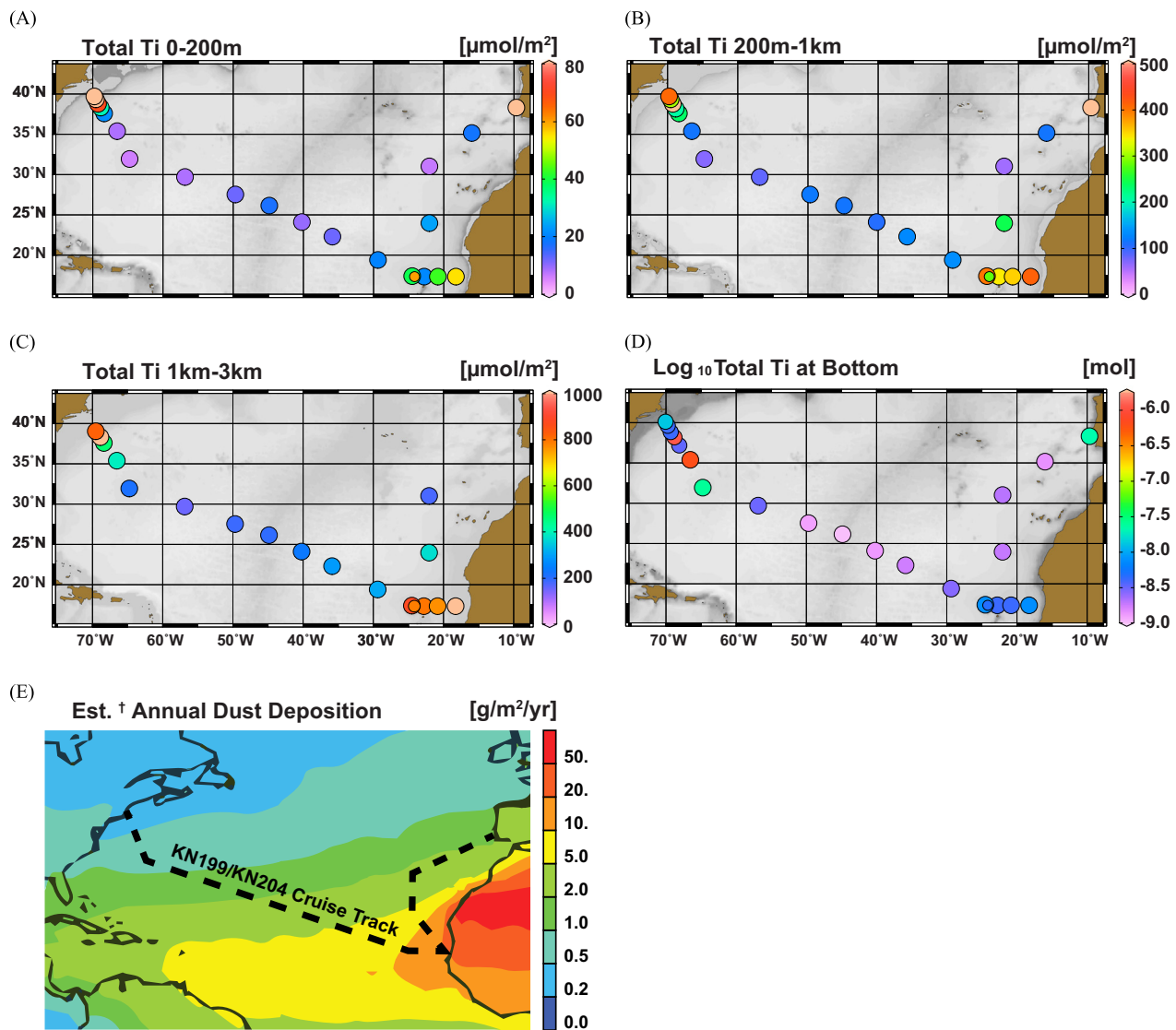
Fig. 9. Station-by-station total (SSF+LSF) particulate Ti inventories in μmol/m² for several depth ranges ((A) 0–200 m; (B) 200 m-1 km; (C) 1–3 km), and particulate Ti concentration at bottom sampling depth ((D), log scale, mol). (†E): Estimated annual dust deposition modified from Jickells et al. (2005) with cruise transects superimposed (dashed black line) for comparison to mesopelagic open ocean inventories (B, C).

biotic community structure that alter export rates (Guidi et al., 2009; Henson et al., 2012; Lam et al., 2011).

The decrease in bulk (SSF+LSF) particle speeds with depth can be explained by the observed decrease in the proportion of faster-sinking LSF particles with depth (Fig. 5; also, Fig. 11c). Depth-dependent increases in settling speeds reported in sediment trap data (Berelson, 2001), are due to such measurements being based on observations of operationally sinking particles, not bulk particles. Assuming SSF particles have a negligible sinking speed (0 m/d), LSF-specific speeds can be calculated from bulk speeds (0–1000 m: 3.5–21 m/d) and the typically observed 80% SSF fractionation below 300 m. These values correspond to LSF sinking speeds of 17–104 m/d, considerably slower than the 150–280 m/d speeds inferred from sediment trap studies in the region (e.g., Ratmeyer et al. 1999; Fischer et al., 1996). Pump-derived LSF particles likely include more slowly sinking large particles, while there is some indication that sediment traps under-collect slowly sinking particles (Haskell et al., 2013). Both biases lead to slower sinking speeds estimated by pumps.

We assess whether horizontal transport of suspended particles should affect our 1D assumption in calculating inventories and residence times. Mean zonal flow in the deep interior (order: 0.1 cm/s; Schott and Stommel, 1978) would necessitate ~5787 d

(almost 16 years) to transit 500 km, the typical distance between our open ocean stations. Even if bulk sinking speeds were as slow as 0.30 m/d (3.4×10^{-4} cm/s), vertical particle sinking should still dominate over horizontal transport, especially at the open ocean stations.

4.8. Lithogenic particle cycling model: conception

Depth profiles of particulate Ti (Fig. 10), an element minimally affected by scavenging and biotic uptake compared to other lithogenic tracers, display consistent features in the open ocean. The SSF (Fig. 10a) exhibits local maxima (10–75 pM) in the mixed layer, minima at the DCM (5–19 pM), and remineralization-like local maxima between 150–500 m depth. Vertical variations in LSF are not as pronounced, though show some of the same features (Fig. 10b). Size-fractionation profiles (Fig. 10c) show that SSF typically accounts for 25–60% of total lithogenics in the upper 100 m, is at a minimum in the DCM (~120 m), then increases rapidly beneath the DCM at all stations to 70–90% by 250–300 m, where it stays relatively constant into the deep ocean. This deep size partitioning is also relatively constant at all stations, despite factors of 2–3 differences in absolute concentrations in SSF and LSF (Fig. 10, lower panels).
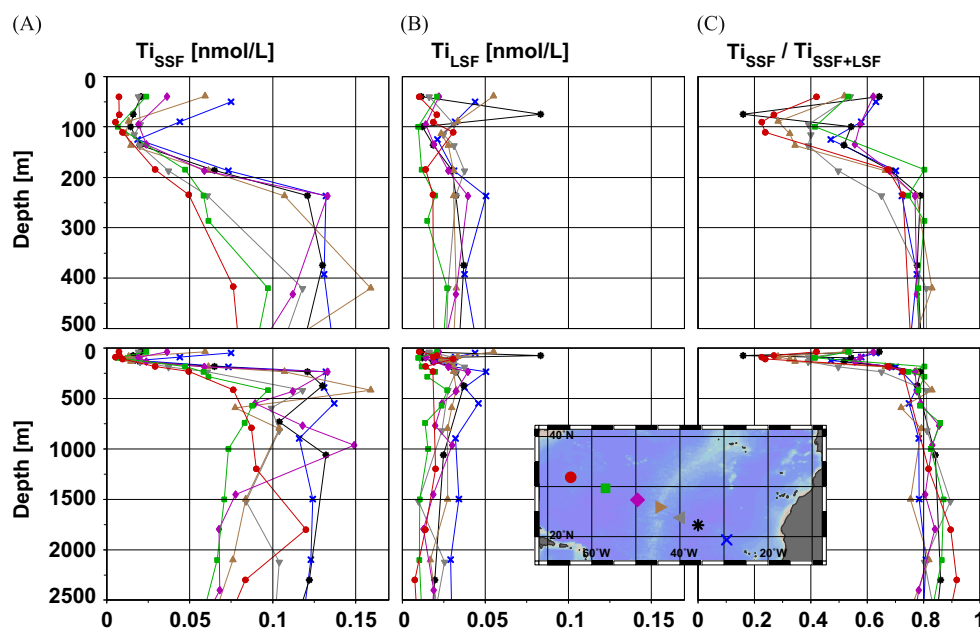
Fig. 10. Particulate Ti profiles for the upper 500 m (top row) and upper 2000 m (bottom row) in the (A) SSF, (B) LSF, and (C) SSF/(SSF+LSF). Only profiles from open ocean stations (inset map, colors and symbols) with minimal laterally-sourced lithogenic influences are shown. (For interpretation of the references to color in this figure legend, the reader is referred to the web version of this article.)
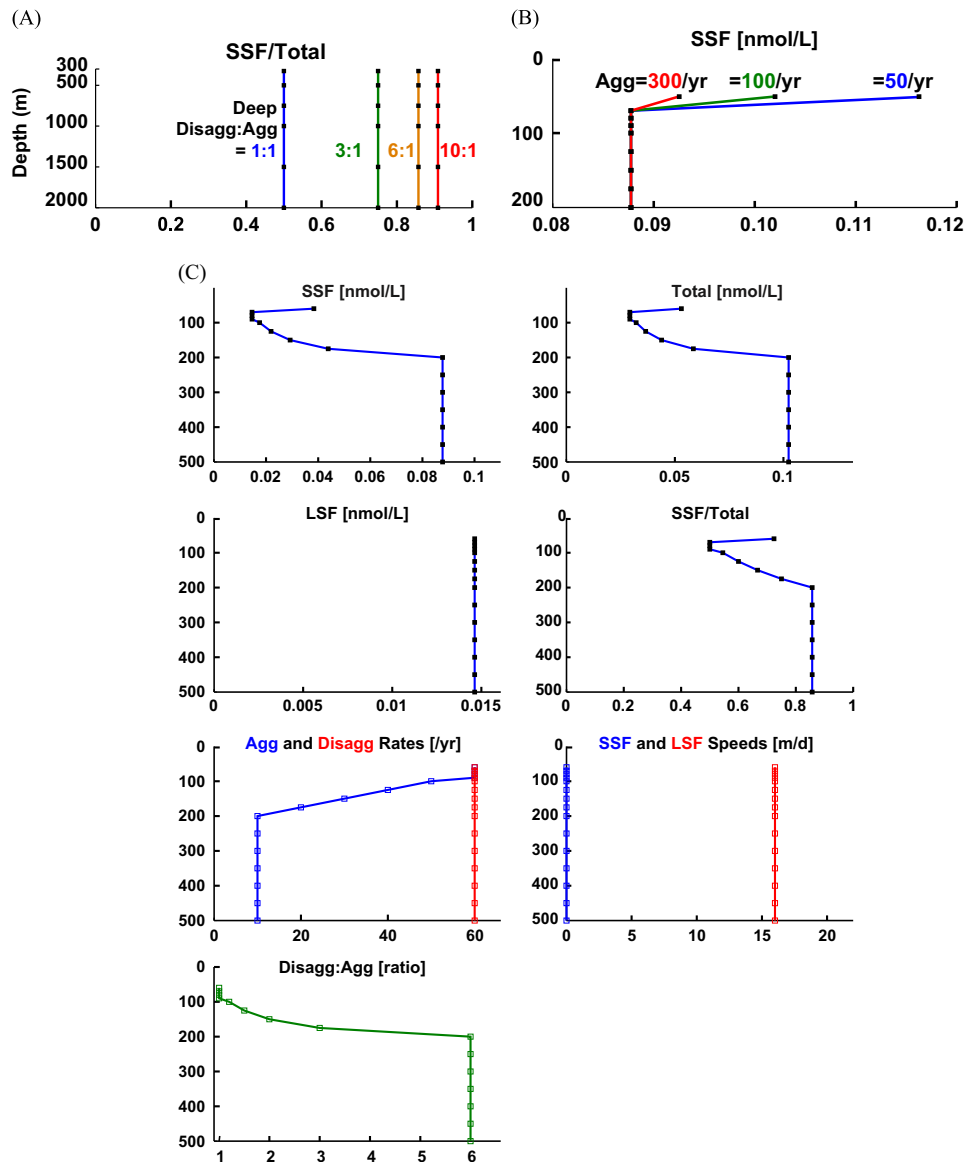
Table 2
Station-by-station inventories (A) of total particulate Ti (SSF+LSF) in three depth ranges (0–200 m, 0–500 m, 0–1000 m), also presented as (B) normalized to the inventory at station 10-09 nearest the Mauritanian margin. Assuming surface-only dust input fluxes (C) estimated from AEROCOM deposition models, we calculate (D) steady state residence times and (E) mean particulate sinking speeds for each depth range.

Station	Location	A: Inventory of total pTi [μmoles/m^2]			B: Relative inventory vs. Mauritania (Stn 10-09) [%]			C: Est. Ti dust flux [μmol/ m^2/d]	D: Dust-relative steady state Res. Time (τ) [d]			E: Dust-relative bulk sinking speed (ω) [m/d]		
		0–200 m	0–500 m	0–1000 m	0–200 m	0–500 m	0–1000 m	Into Surface	0–200 m	0–500 m	0–1000 m	0–200 m	0–500 m	0–1000 m
11-01	Woods Hole	82	198	492	149	89	106	0.160	512	1233	3073	0.4	0.4	0.3
11-02		301	438	604	547	196	130	0.160	1881	2734	3770	0.1	0.2	0.3
11-03		69	253	583	125	113	125	0.160	431	1579	3643	0.5	0.3	0.3
11-04		32	104	246	58	46	53	0.160	198	646	1534	1.0	0.8	0.7
11-06		21	138	253	38	62	54	0.160	132	860	1580	1.5	0.6	0.6
11-08		8.3	39	122	15	17	26	0.160	52	243	761	3.9	2.1	1.3
11-10	Bermuda	6.5	28	73	12	12	16	0.256	25	108	285	7.9	4.6	3.5
11-12		8.5	38	88	15	17	19	0.320	27	118	274	7.5	4.2	3.6
11-14	MAR	12	56	127	23	25	27	0.480	26	117	264	7.7	4.3	3.8
11-16	MAR	17	64	127	30	29	27	0.641	26	100	199	7.6	5.0	5.0
11-18		10	46	111	18	21	24	1.121	9	41	99	23	12	10
11-20		12	59	140	22	26	30	1.602	8	37	87	26	14	11
11-22		20	72	153	36	32	33	3.203	6	22	48	32	22	21
11-24	CVI 2011	60	173	340	109	78	73	4.805	12	36	71	16	14	14
10-12	CVI 2010	39	167	435	70	75	93	4.805	8	35	91	25	14	11
10-11		21	131	358	38	59	77	5.765	4	23	62	55	22	16
10-10		43	185	393	77	83	85	6.406	7	29	61	30	17	16
10-09	Mauritania	55	223	465	100	100	100	6.406	9	35	73	23	14	14
10-07		24	127	264	43	57	57	2.562	9	50	103	22	10	9.7
10-05		6.7	24	63	12	11	14	0.961	7	25	66	29	20	15
10-03		18	61	131	32	27	28	0.641	28	94	204	7.2	5.3	4.9
10-01	Lisbon	131	367	187	238	165	40	0.320	410	1146	584	0.5	0.4	1.7

Strong partitioning of lithogenic material to the LSF in the surface despite delivery of dust into the SSF (Ratmeyer et al., 1999) suggests the importance of aggregation processes in the shallow ocean. This is confirmed by XRF images of micron-scale lithogenic particles in the LSF from the mixed layer (Fig. 6). Short residence times of lithogenic particles in the surface (Table 2) indicate that aggregation of fine, eolian dust into LSF and its subsequent removal occur rapidly. The low concentrations of lithogenic elements in the DCM (Fig. 6, ML, DCM; Fig. 11) show that lithogenic particles deposited in the mixed layer efficiently

bypass the DCM as they are transported to depth. The DCM is thus a "lithogenic shadow zone" where removal processes (aggregation and sinking) dominate over sources (disaggregation of LSF).

Beneath the euphotic zone (Fig. 6, OMZ), we observe both lithogenic-rich and lithogenic-poor aggregates, presumably from the mixed layer and the DCM, respectively. In the 150–400 m depth range, below the DCM, large aggregates begin to disaggregate, leading to a rapid increase in SSF lithogenic particles (Fig. 10c). An analogous release of micron-scale mineral particles from the LSF to

Fig. 11. 1-D lithogenic cycling model responses and results. Scenario parameters are itemized in Table 3, with details about model configurations discussed in the text. (A) Varying the deep ocean (z > 300 m) disagg:agg rate ratio from (1:1 to 10:1, colored traces) increases the size-fractionation (SSF:Total) of lithogenics towards the SSF. (B) Varying the absolute mean aggregation rate between 50 yr^{-1} and 300 yr^{-1} (colored traces) primarily affects the mixed layer (upper point, plotted at 60 m) SSF concentration. (C) Allowing aggregation rates to increase towards the surface (bottom panels; aggregation increasing to 60 yr^{-1} above 100 m) generates lithogenic concentration and size-fraction profiles remarkably similar to those observed in the ocean (cf. Fig. 10). (D) Imparting an SSF settling speed of 0.5 m/d generates slight curvature in the LSF profile at shallow depths, smoothes both SSF and LSF profiles, and only slightly decreases the steady-state lithogenic inventory (cf. Fig. 11c). (E) Allowing the LSF sinking speed to increase with depth (from 16 to 20 m/d in the lower 2000 m; bottom panels) decreases the total Ti inventory at those depths proportionally. (F) Imparting a time-varying dust input generates time-varying dust responses in both size-fractions. Animated versions of these outputs are available in the Supplemental data.

SSF as a result of particle disaggregation and remineralization has been observed for barite (Bishop, 1988). Longer SSF residence times in the sub-euphotic zone (Table 2) than in the mixed layer thus create the strongest and most consistently observed lithogenic metal gradients at depths below, rather than above, the DCM, even in this region of unparalleled dust input fluxes.

Large but rare aggregates containing fine lithogenic particles are also observed in deep samples (Fig. 6, deep interior), many of which are likely fast-sinking, dust-containing fecal pellets generated by zooplankton.

Taken as a whole, shallow aggregation, large particle sinking, and deep disaggregation appear to be the dominant processes controlling the vertical distribution and cycling of lithogenic metals in the open ocean.

4.9. Lithogenic particle cycling model: description and parameters

We can express the conceptual model of lithogenic cycling described above as a 1-D box model of Ti in which we can test parameter sensitivities and generate estimates for particle disaggregation/aggregation and sinking speeds.

We first assume that aggregation and disaggregation are the major drivers of lithogenic particle partitioning between the SSF and the LSF in the upper ocean. We also assume that all Ti entering the system does so as fine (SSF) eolian material into the mixed layer, supported by the fact that LSF (> 51 μm) inputs of Ti, though not unheard of as far as Cape Verde (Chiapello et al., 1997; Rognon et al., 1996), are rarely considered relevant to the open ocean (Huneeus et al., 2011; Shelley et al., 2015). We finally assume that
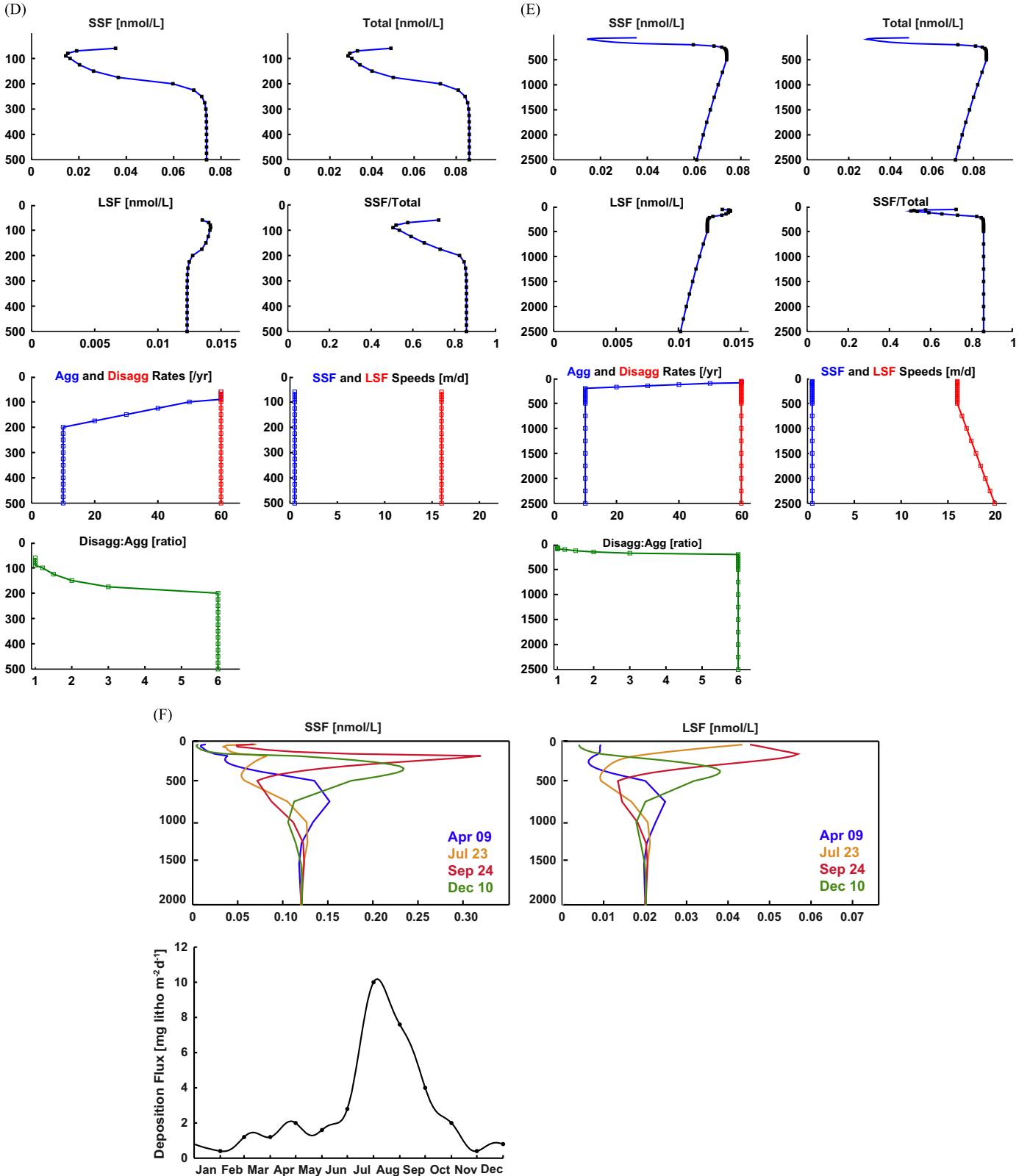
Fig. 11. (*continued*)

gravity-driven sinking of large particles is the primary vertical transport mechanism, and that horizontal transport is negligible.

We can thus describe any 1-D pair of SSF and LSF profiles using a stacked multi-box model in which, for any box i, the change in concentration of the two size fractions is described by a pair of first-order, ordinary differential equations (ODEs):

$$\frac{d\,\mathrm{SSF}_i}{dt} = F_{dust,i} + \beta_{-2,i}\,\mathrm{LSF}_i - \beta_{2,i}\,\mathrm{SSF}_i - \frac{\omega_{SSF,i}}{Z}\mathrm{SSF}_i + \frac{\omega_{SSF,i-1}}{Z_{i-1}}\mathrm{SSF}_{i-1}$$

(1)

$$\frac{d\,\text{LSF}_i}{dt} = \beta_{2,i}\,\text{SSF}_i - \beta_{-2,i}\,\text{LSF}_i - \frac{\omega_{\text{LSF},i}}{Z_i}\text{LSF}_i + \frac{\omega_{\text{LSF},i-1}}{Z_{i-1}}\text{LSF}_{i-1} \qquad (2)$$

The sole input of Ti is the local dust flux (F_{dust}), which is entirely into the SSF of the mixed layer, the shallowest box. Aggregation and disaggregation between the SSF and LSF are described by the first-order rate constants β_2 and β_{-2}, respectively; and vertical transport of SSF and LSF particles between depths is attributable to their sinking speeds ω_{SSF} and ω_{LSF}, respectively, which are effectively converted to rates by dividing by the thickness (Z) of each box. Differential equations were solved using a Runge–Kutte ODE45 parameterization in MATLAB (Math-Works, Natick MA). For all scenarios presented, the model was started with zero-inventory (empty water column) and run for 20 years, which was shown by comparison to 200 and 2000 year runs to have reached steady state.

This is a simplified version of the conceptual models used to model scavenging and removal by particles of thorium isotopes (Clegg and Whitfield, 1993; Clegg et al., 1991; Marchal and Lam, 2012) but retaining the particle dynamics terms only. We postulate that since particulate Ti is highly refractory in the water column, we can ignore the scavenging and remineralization terms that transfer Ti between dissolved and SSF pools in such models. Preliminary weak leachable Ti fractions (not shown) from the Mauritanian transect were typically < 1% of the total Ti signal, confirming that neglecting Ti scavenging is a minimal source of error.

During our transect, the typical thickness of the mixed layer was 60 m, which we use as the thickness of the surface box in all scenarios. All boxes are well mixed and are spaced below the mixed layer to highlight general profile behaviors: every 10 m between 60 and 100 m, every 25 m between 100 and 300 m, and as necessary > 300 m (e.g. to follow feature propagation in long/deep model runs.). In model outputs, values are plotted at the bottom of the box (e.g. mixed layer at 60 m).

4.10. Lithogenic particle cycling model: sensitivities and results

We use the model to test the sensitivities of the SSF Ti, LSF Ti and their size-fractionation profiles to variations in rates. Model scenarios and key parameters are summarized in Table 3.

We first assume a constant dust input flux of 2 mg/m²/d, which approximates the mean annual eolian deposition observed at Bermuda (Jickells et al., 1998). Assuming a Ti:Al mass ratio of 0.07, typical of African dust collected between Cape Verde and Mauritania (Stuut, 2005), and an Al crustal weight abundance of 8% (Taylor and McLennan, 1995), this yields an input F_{dust} of 270 nmol Ti$_{\text{SSF}}$/m²/d into the mixed layer.

For our first three scenarios (Figs. 11a-c; Table 3), we assign the SSF a zero sinking speed ($\omega_{\text{SSF}}=0$ m/d) and the LSF a sinking speed of $\omega_{\text{LSF}}=16$ m/d, consistent with sinking speeds estimated for

large aggregates by using video plankton recorder (VPR) images and gel traps near Bermuda (McDonnell and Buesseler, 2012), and vary aggregation and disaggregation rate constants.

Published estimates for aggregation and disaggregation rate constants are typically derived from inverse models of thorium isotope (^{234}Th, ^{228}Th, ^{230}Th) and particle concentration profiles or fluxes, usually below the euphotic zone (e.g. Murnane et al., 1996; Cochran et al., 2000). Compilations of rate constant estimates show large spatiotemporal variabilities and uncertainties (Marchal and Lam, 2012), though disaggregation rate constants (disagg.: 1–1000 yr^{-1}) are generally greater than aggregation rate constants (agg.: 0.1–100 yr^{-1}), consistent with the deep ocean being dominated by remineralization, disaggregation, and fragmentation of large aggregates rather than their production.

In scenario A, we examine size partitioning (SSF/Total) in several model outputs for $z > 300$ m in which the disagg:agg ratio is held constant throughout the water column (Fig. 11a; Table 3). When the disagg:agg ratio is 1:1, refractory lithogenics partition evenly between the SSF and LSF (Fig. 11a, blue line). Increasing the disagg:agg ratio increases lithogenic partitioning to the SSF (Fig. 11a, non-blue lines). Below 300 m in the N. Atlantic we observe general lithogenic partitioning of 75–85% SSF (Fig. 10c), which corresponds to a modeled rate ratio between 3:1 to 6:1. For a fixed LSF sinking speed, the disagg:agg ratio of the deep ocean is the primary control of lithogenic size-fractionation.

In scenario B, we examine the sensitivity of SSF Ti concentrations to absolute rates of aggregation (Table 3) in the upper 200 m. We hold the disagg:agg ratio constant at 6:1 through the entire water column, which best reproduced observed size-fractionation below 300 m, and vary the absolute aggregation rate constant from 50 yr^{-1} to 300 yr^{-1}. There is a surface maximum in SSF Ti at all aggregation rate constants because of the dust input flux to this box, but the primary effect of increased absolute aggregation rates is a decreased mixed layer lithogenic inventory (Fig. 11b). Aggregation rates that are too low relative to dust inputs lead to modeled surface inventories that are too large (and vice versa), suggesting a constraint exists to this parameter in surface waters given measurements of surface inventories and estimates of lithogenic input fluxes and particle settling speeds.

In scenario C, the disagg:agg ratio is held constant at 6:1 below 200 m, but decreases to 1:1 at the surface (Fig. 11c; Table 3). We hold disaggregation constant at 60 yr^{-1} and aggregation at 10 yr^{-1} below 200 m, but allow aggregation to increase monotonically above 200 m, reaching equivalence with disaggregation (60 yr^{-1}) between 0 and 100 m (Fig. 11c, lower panels). This choice to vary aggregation rather than disaggregation is somewhat arbitrary, though for demonstrative purposes, biotic aggregation may be reasonably assumed to be stronger nearer the mixed layer. We find that by varying only three rate constant parameters and imposing a reasonable aggregation rate profile shape, modeled lithogenic size partitioning and concentration profiles similar to

Table 3
Model sensitivity experiments: model parameters and sensitivity tests used in various scenarios described in the text.

Scenario	Dust flux (mg/m²/d)	ω_{LSF} (m/d)	ω_{SSF} (m/d)	Disagg:agg (ratio)	Agg (1/y)	Sensitivities examined
A	2	16	0	Varying from 1:1 to 10:1	N/A	SSF/Total for $z > 300$
B	2	16	0	6:1	Varying from 50 to 300	SSF Ti in mixed layer
C	2	16	0	Increasing from surface (1:1) to 200 m; constant (6:1) below 200 m	Decreasing from 60 at surface to 10 at 200 m; 10 below 200 m	Profile shapes of SSF, LSF, and SSF/Total
D	2	16	0.5	Same as #3	Same as #3	Profile shapes of SSF, LSF, and SSF/Total
E	2	16, but increasing from 16 to 20 below 500 m	0.5	Same as #3	Same as #3	LSF, Total Ti
F	Seasonally varying	16	0.1	Same as #3	Similar to #3, but 30 below 200 m	Time evolution of SSF and LSF profiles

those observed in the western basin (Fig. 10) emerge: upper water-column LSF dominance and a sub-mixed layer minimum in SSF particles, consistent with Dammshäuser and Croot (2012).

Using scenario C as a base, we now allow sinking speeds to vary. In scenario D, we allow the SSF to sink slowly (Table 3), keeping in mind that fine/SSF bulk speeds likely have a smaller range of variability than those of large/LSF particles. Allowing fine particles to settle as rapidly as 0.5 m/d (Fig. 11d) only slightly bows the LSF profile and smoothes all profiles. This smoothing effect is primarily observed just below the mixed layer where SSF gradients are greatest. Fine particles settling out of the mixed layer, even at these speeds, notably fail to eliminate the DCM "lithogenic shadow zone".

In scenario E, LSF speed is monotonically increased from 16 to 20 m/d in the bottom 2000 m, decreasing total Ti inventories at corresponding depths (Fig. 11e; Table 3). Faster LSF speeds rapidly decrease the steady-state concentration of the LSF, which directly reduces lithogenic residence times and total lithogenic abundances. If this effect is water-column wide, i.e. if LSF sinking speeds are positively correlated with absolute dust inputs (due to an increase in lithogenic ballasting), standing lithogenic particle inventories would thus be comparatively smaller than expected based on input fluxes alone. This may be the case in the eastern North Atlantic, where marine Ti inventories are only two- to three-fold greater than in the western basin (Table 2) despite a more than seven-fold relative increase in dust inputs.

In scenario F, we impose temporally varying dust inputs. We start with a scenario similar to scenario D: sinking speeds of 16 m/d for LSF and 0.1 m/d for SSF, with a similar near-surface aggregation rate shape. We impose slightly higher overall rates: 30 yr^{-1} for deep aggregation and 180 yr^{-1} for disaggregation below 300 m and then assign a seasonal dust input flux with a strong summer maximum (Fig 11f, lower panels; Table 3). This input flux is derived from monthly deposition estimates of the "Aerocom_Median" model near Bermuda (AEROCOM Phase II, 2013) fitted using a continuous, smooth sum of sines interpolation to simplify model ODE solutions. The seasonal input flux bears strong similarity in shape to the seasonal patterns of lithogenic element fluxes observed at the L1 sediment trap site ~600 km NW of the Canary Islands (Kuss et al., 2010). Several snapshots in the 20th model year are presented in Fig. 11f and in animated form in the Supplemental materials.

Lithogenic profiles now exhibit time-varying responses to seasonal dust forcing. Mixed layer concentrations exhibit maxima simultaneous with maximum dust flux in July. The annual dust pulse then propagates downwards, with sub-euphotic concentrations reaching maxima in late September. Net propagation speeds of the pulse are nearest to LSF speeds (16 m/d) in the surface, where partitioning to the LSF is highest, then slow to reflect the increased relative abundance of fine SSF material (SSF speed: 0.1 m/d) at depth. By December, the summer dust pulse is seen as a maximum around 500 m. Both size fraction maxima continue to relax and disperse vertically throughout the winter into the spring (April). Revisiting the annual dust event (July), the remnant of the previous year's dust pulse remains visible at 1000 m. This > 1 year lag (to 1000 m) in lithogenic pulsing is much greater than the 1.5 month lag (to 2000 m) observed by Brust et al. (2011) in sediment trap data NW of the Canary Islands. Two (or multiple) subsurface maxima in lithogenic material can be generated using only 1-D packaging/sinking processes and time-varying dust inputs.

Sinking speeds determine the vertical propagation rates, and deep aggregation rate constants determine the amplitudes of input pulses through the water column. Greater aggregation rates and faster speeds thus lead to a wider dynamic range of lithogenic concentration variations for a temporally varying input. Variations in LSF concentrations predicted by such scenarios could be observable in field data using repeated measurements of concentration profiles, but may also be visible in time series sediment trap fluxes.

Previously calculated residence times suggest that the water column maintains an inventory of both short-term (days to weeks) and long-term (months to years) lithogenic inputs depending on the depth of integration. Given estimates or measurements of lithogenic input fluxes, this model suggests it is possible to use suspended lithogenic particles to examine many important bulk marine (aggregation, disaggregation and sinking) and atmospheric (dust deposition) processes that alter lithogenic inventories. Our model also suggests that temporal variations in lithogenic inputs to the ocean may impart notable signals, dependent on true marine parameters/rates, in repeated observations of refractory particle profiles.

4.11. Applicability of the lithogenic particle model to POC cycling

Our modeling of an inert lithogenic tracer provides a starting point for directly examining the dynamic particle processes that control general particle cycling. Many such parameters, including aggregation/disaggregation and sinking speeds, are relevant to the biological pump and thus carbon and bioactive trace metal cycling, but are difficult to measure directly. How applicable is such a lithogenic cycling model to the biological pump with respect to particulate organic carbon (POC) cycling?

At one extreme, we can imagine that POC behaves exactly like lithogenic particles with respect to aggregation, disaggregation, and sinking in the near-surface, but that it also experiences significant remineralization into the dissolved phase, a process less important for lithogenics. Two-particle-box models of POC and Th dynamics often add such a remineralization loss term from small particles (e.g. Clegg et al., 1991). In surface waters, we observed POC to be partitioned less strongly to the LSF than lithogenics (10–60% LSF for POC compared to 50–80% LSF for lithogenics; Lam et al., 2015). This implies a need to account for an additional remineralization term between fine and coarse size fractions to account for remineralization or assimilation of POC by zooplankton during aggregation into large > 51 μm particles.

The other extreme—that POC behaves nothing at all like lithogenic particles—is unlikely considering that the aggregation and disaggregation processes acting on lithogenics are presumably biologically mediated and driven by POC consumption, production, and packaging. Key differences in size distributions for POC compared to lithogenics may, however, alter the effective aggregation rates experienced by POC compared to lithogenic pools. Fine lithogenics have a narrower particle size spectrum in the 1–20 μm-range, if sourced completely from dust (Ratmeyer et al., 1999; Stuut, 2005), compared to POC which spans the full range of sizes from organic polymers, viruses, bacteria, pico- and nano-plankton, etc. (McCave, 1984; Lal, 1977). Such organic pools, when operationally split into > 51 μm and < 51 μm fractions, may aggregate/disaggregate fundamentally differently than lithogenics. Our dataset and model results suggest that the processes driving POC and lithogenic size-partitioning are strongly linked, but further mechanistic investigation is needed to determine how applicable lithogenic-derived or constrained agg/disagg/sinking rate estimates are to POC and other particulate tracers.

5. Conclusions

The distributions of size-fractionated lithogenic metals Al, Fe, and Ti in the North Atlantic reflect the intensity and extent of both atmospheric and lateral lithogenic inputs as well as key

oceanographic processes such as scavenging, biotic uptake, aggregation, disaggregation, and vertical sinking. In the upper ocean, lithogenics are demonstrated to have strong, rapid packaging into the $> 51\ \mu m$ size-fraction within the mixed layer, minimal abundances just below the mixed layer at the DCM, and concentration maxima in the upper mesopelagic. Lateral, hydrothermal, and benthic sources act as intense, locally-important inputs of Al, Fe, and Ti at some stations, with African dust input ratios dominating lithogenic particle composition across most of the basin's interior. A two size-fraction, 1-D box model of particulate Ti that includes terms for dust inputs, aggregation and disaggregation between size fractions, and vertical sinking, can successfully describe observed lithogenic distributions and demonstrates the range of effects that parameter and input variations have on size-fractionated lithogenic profiles. In combination with atmospheric dust models, water column lithogenic inventories may be useful indicators of eolian deposition patterns as imprinted upon and reworked by the marine biological pump, perhaps eventually helping to constrain the functioning of both.

Acknowledgments

Appendix A. Supporting information

Supplementary data associated with this article can be found in the online version at http://dx.doi.org/10.1016/j.dsr2.2014.11.019.

References

AEROCOM Phase II, 2013. Interface. Available from: ⟨http://aerocom.met.no⟩ (accessed 17.08.13).

Berelson, W.M., 2001. Particle settling rates increase with depth in the ocean. Deep-Sea Res. II 49 (1), 237–251.

Biscaye, P.E., Eittreim, S.L., 1977. Suspended particulate loads and transports in the nepheloid layer of the abyssal Atlantic Ocean. Mar. Geol. 23 (1), 155–172.

Bishop, J., 1988. The barite–opal–organic carbon association in oceanic particulate matter. Nature 332, 24.

Bloemsma, M.R., Zabel, M., Stuut, J.B.W., Tjallingii, R., Collins, J.A., Weltje, G.J., 2012. Modelling the joint variability of grain size and chemical composition in

sediments. Sediment. Geol., 1–14. http://dx.doi.org/10.1016/j.sedgeo.2012.04.009.

Bory, A., Jeandel, C., Leblond, N., Vangriesheim, A., Khripounoff, A., Beaufort, L., Rabouille, C., Nicolas, E., Tachikawa, K., Etcheber, H., 2001. Downward particle fluxes within different productivity regimes off the Mauritanian upwelling zone (EUMELI program). Deep-Sea Res. I 48 (10), 2251–2282.

Bower, A., Lozier, S., Gary, S., 2011. Deep-Sea Res. II 58 (17–18), 1798–1818. http://dx.doi.org/10.1016/j.dsr2.2010.10.060.

Boyle, E.A., 1983. Chemical accumulation variations under the Peru Current during the past 130,000 years. J. Geophys. Res.: Oceans 88 (C12), 7667–7680.

Boyle, E.A., Bergquist, B.A., Kayser, R.A., Mahowald, N., 2005. Iron, manganese, and lead at Hawaii Ocean Time-series station ALOHA: temporal variability and an intermediate water hydrothermal plume. Geochim. Cosmochim. Acta 69 (4), 933–952. http://dx.doi.org/10.1016/j.gca.2004.07.034.

Brewer, P.G., Spencer, D.W., Biscaye, P.E., Hanley, A., Sachs, P.L., Smith, C.L., Kadar, S., Fredericks, J., 1976. The distribution of particulate matter in the Atlantic Ocean. Earth Planet. Sci. Lett. 32 (2), 393–402.

Bruland, K.W., Rue, E.L., Smith, G.J., DiTullio, G.R., 2005. Iron, macronutrients and diatom blooms in the Peru upwelling regime: brown and blue waters of Peru. Mar. Chem. 93 (2–4), 81–103. http://dx.doi.org/10.1016/j.marchem.2004.06.011.

Brust, J., Schulz-Bull, D.E., Leipe, T., Chavagnac, V., Waniek, J.J., 2011. Descending particles: from the atmosphere to the deep ocean—a time series study in the subtropical NE Atlantic. Geophys. Res. Lett 38 (6), http://dx.doi.org/10.1029/2010GL045399.

Carr, M.E., 2002. Estimation of potential productivity in Eastern Boundary Currents using remote sensing. Deep-Sea Res. II 49 (1–3), 59–80.

Chiapello, I., Bergametti, G., Chatenet, B., Bousquet, P., Dulac, F., Soares, E.S., 1997. Origins of African dust transported over the northeastern tropical Atlantic. J. of Geophys. Res.—Atmos. 102 (D12), 13701–13709.

Clegg, S.L., Bacon, M.P., Whitfield, M., 1991. Application of a generalized scavenging model to thorium isotope and particle data at equatorial and high-latitude sites in the Pacific Ocean. J. Geophys. Res.: Oceans 96 (C11), 20655–20670.

Clegg, S.L., Whitfield, M., 1993. Application of a generalized scavenging model to time series 234 Th and particle data obtained during the JGOFS North Atlantic bloom experiment. Deep-Sea Res. I 40 (8), 1529–1545.

Cochran, J.K., Buesseler, K.O., Bacon, M.P., Wang, H.W., Hirschberg, D.J., Ball, L., Andrews, J., Crossin, G., Fleer, A., 2000. Short-lived thorium isotopes (234Th, 228Th) as indicators of POC export and particle cycling in the Ross Sea, Southern Ocean. Deep-Sea Res. II 47 (15), 3451–3490.

Croot, P.L., Heller, M.I., 2012. The importance of kinetics and redox in the biogeochemical cycling of iron in the surface ocean. Front. Microbiol. 3, http://dx.doi.org/10.3389/fmicb.2012.00219.

Cutter, G., Andersson, P., Codispoti, L., Croot, P., François, R., Lohan, M.C., Obata, H., Rutgers v. d. Loeff, M., 2010. Sampling and Sample-Handling Protocols for GEOTRACES Cruises. ⟨http://www.geotraces.org/libraries/documents/Intercalibration/Cookbook.pdf⟩.

Dale, A.W., Sommer, S., Ryabenko, E., Noffke, A., Bohlen, L., Wallmann, K., Stolpovsky, K., Greinert, J., Pfannkuche, O., 2014. Benthic nitrogen fluxes and fractionation of nitrate in the Mauritanian oxygen minimum zone (Eastern Tropical North Atlantic). Geochim. Cosmochim. Acta 134(C), 234–256. http://dx.doi.org/10.1016/j.gca.2014.02.026.

Dammshäuser, A., Wagener, T., Croot, P.L., 2011. Surface water dissolved aluminum and titanium: tracers for specific time scales of dust deposition to the Atlantic? Geophys. Res. Lett. 38 (24), http://dx.doi.org/10.1029/2011GL049847.

Dammshäuser, A., Croot, P.L., 2012. Low colloidal associations of aluminium and titanium in surface waters of the Tropical Atlantic. Geochim. Cosmochim. Acta 96, 304–318. http://dx.doi.org/10.1016/j.gca.2012.07.032.

Dammshäuser, A., Wagener, T., Garbe-Schönberg, D., Croot, P., 2013. Particulate and dissolved aluminum and titanium in the upper water column of the Atlantic Ocean. Deep-Sea Res. I 73(C), 127–139. http://dx.doi.org/10.1016/j.dsr.2012.12.002.

Davies, G.R., Cliff, R.A., Norry, M.J., Gerlach, D.C., 1989. A Combined Chemical and Pb–Sr–Nd Isotope Study of the Azores and Cape Verde Hot-spots: The Geodynamic Implications, vol. 42. Geological Society, London, pp. 231–255. http://dx.doi.org/10.1144/GSL.SP.1989.042.01.15 (Special Publications).

Diekmann, B., Fütterer, D.K., Grobe, H., Hillenbrand, C.D., Kuhn, G., Michels, K., Petschick, R., Pirrung, M., 2004. Terrigenous Sediment Supply in the Polar to Temperate South Atlantic: Land–Ocean Links of Environmental Changes During the Late Quaternary, pp. 375–399.

Dunne, J.P., Sarmiento, J.L., Gnanadesikan, A., 2007. A synthesis of global particle export from the surface ocean and cycling through the ocean interior and on the seafloor. Glob. Biogeochem. Cycles 21 (4), GB4006. http://dx.doi.org/10.1029/2006GB002907.

Dymond, J., Collier, R., Mcmanus, J., Honjo, S., Manganini, S., 1997. Can the aluminum and titanium contents of ocean sediments be used to determine the paleoproductivity of the oceans? Paleoceanography 12 (4), 586–593.

Fischer, G., Donner, B., Ratmeyer, V., Davenport, R., Wefer, G., 1996. Distinct year-to-year particle flux variations off Cape Blanc during 1988–1991: relation to delta O-18-deduced sea-surface temperatures and trade winds. J. Mar. Res. 54 (1), 73–98.

Fischer, G., Karakaş, G., 2009. Sinking rates and ballast composition of particles in the Atlantic Ocean: implications for the organic carbon fluxes to the deep ocean. Biogeosciences 6 (1), 85–102.

Fischer, G., Reuter, C., Karakaş, G., Nowald, N., Wefer, G., 2009. Offshore advection of particles within the Cape Blanc filament, Mauritania: results from observational

and modelling studies. Prog. Oceanogr. 83 (1), 322–330. http://dx.doi.org/10.1016/j.pocean.2009.07.023.

Fitzsimmons, J.N., Zhang, R., Boyle, E.A., 2013. Dissolved iron in the tropical North Atlantic Ocean. Mar. Chem. 154, 87–99. http://dx.doi.org/10.1016/j.marchem.2013.05.009.

Francois, R., Honjo, S., Krishfield, R., Manganini, S., 2002. Factors controlling the flux of organic carbon to the bathypelagic zone of the ocean. Glob. Biogeochem. Cycles 16 (4), 34-1–34-20. http://dx.doi.org/10.1029/2001GB001722.

German, C.R., von Damm, K.L., 2006. Hydrothermal Processes, The Oceans & Marine Geochemistry (Treatise on Geochemistry Series, vol. 6. Elsevier-Pergamon, Oxford, pp. 181–222.

Ginoux, P., Prospero, J.M., Torres, O., Chin, M., 2004. Long-term simulation of global dust distribution with the GOCART model: correlation with North Atlantic Oscillation. Environ. Model. Softw. 19 (2), 113–128. http://dx.doi.org/10.1016/S1364-8152(03)00114-2.

Guidi, L., Stemmann, L., Jackson, G.A., Ibanez, F., Claustre, H., Legendre, L., Picheral, M., Gorsky, G., 2009. Effects of phytoplankton community on production, size and export of large aggregates: a world-ocean analysis. Limnol. Oceanogr. 54 (6), 1951.

Haskell, W.Z.I., Berelson, W.M., Hammond, D.E., Capone, D.G., 2013. Particle sinking dynamics and POC fluxes in the Eastern Tropical South Pacific based on Th-234 budgets and sediment trap deployments. Deep-Sea Res. I 81, 1–13. http://dx.doi.org/10.1016/j.dsr.2013.07.001.

Henson, S.A., Sanders, R., Madsen, E., 2012. Global patterns in efficiency of particulate organic carbon export and transfer to the deep ocean. Glob. Biogeochem. Cycles 26 (1), http://dx.doi.org/10.1029/2011GB004099.

Huneeus, N., Schulz, M., Balkanski, Y., Griesfeller, J., PROSPERO, J., Kinne, S., Bauer, S., Boucher, O., CHIN, M., Dentener, F., Diehl, T., Easter, R., Fillmore, D., Ghan, S., Ginoux, P., Grini, A., Horowitz, L., Koch, D., Krol, M.C., Landing, W., Liu, X., Mahowald, N., Miller, R., Morcrette, J.J., Myhre, G., Penner, J., Perlwitz, J., Stier, P., Takemura, T., Zender, C.S., 2011. Global dust model intercomparison in Aero-Com phase I. Atmos. Chem. Phys. 11 (15), 7781–7816. http://dx.doi.org/10.5194/acp-11-7781-2011.

Iversen, M.H., Ploug, H., 2010. Ballast minerals and the sinking carbon flux in the ocean: carbon-specific respiration rates and sinking velocity of marine snow aggregates. Biogeosciences 7 (9), 2613–2624. http://dx.doi.org/10.5194/bg-7-2613-2010.

Jackson, M.G., Hart, S.R., Saal, A.E., Shimizu, N., Kurz, M.D., Blusztajn, J.S., Skovgaard, A.C., 2008. Globally elevated titanium, tantalum, and niobium (TITAN) in ocean island basalts with high 3He/4He. Geochem. Geophys. Geosyst. 9 (4), Q04027. http://dx.doi.org/10.1029/2007GC001876.

Jenkins, W.J., Smethie, W.M., Boyle, E.A., Cutter, G.A., 2015. Water mass analysis for the U.S. GEOTRACES North Atlantic Sections. Deep-Sea Research II: Topical Studies in Oceanography 116, 6–20. http://dx.doi.org/10.1016/j.dsr2.2014.11.018.

Jickells, T.D., Dorling, S., Deuser, W.G., Church, T.M., Arimoto, R., Prospero, J.M., 1998. Air-borne dust fluxes to a deep water sediment trap in the Sargasso Sea. Glob. Biogeochem. Cycles 12 (2), 311–320.

Jickells, T.D., An, Z.S., Andersen, K.K., Baker, A.R., Bergametti, G., Brooks, N., Cao, J.J., Boyd, P.W., Duce, R.A., Hunter, K.A., 2005. Global iron connections between desert dust, ocean biogeochemistry, and climate. Science 308 (5718), 67–71. http://dx.doi.org/10.1126/science.1105959.

Knudsen, M.F., Abrahamsen, N., Riisager, P., 2005. A rock-and palaeomagnetic study of geologically recent lavas and 1995 volcanic glass on Fogo (Cape Verde Islands). Bull. Geol. Soc. Denmark 52, 39–52.

Kuss, J., Kremling, K., 1999a. Particulate trace element fluxes in the deep northeast Atlantic Ocean. Deep-Sea Res. I 46 (1), 149–169.

Kuss, J., Kremling, K., 1999b. Spatial variability of particle associated trace elements in near-surface waters of the North Atlantic (30N/60W to 60N/2W), derived by large volume sampling. Mar. Chem. 68 (1–2), 71–86.

Kuss, J., Waniek, J.J., Kremling, K., Schulz-Bull, D.E., 2010. Deep-Sea Res. I 57 (6), 785–796. http://dx.doi.org/10.1016/j.dsr.2010.04.002.

LaCasce, J.H., Speer, K.G., 1999. Lagrangian statistics in unforced barotropic flows. J. Mar. Res. 57 (2), 245–274.

Lal, D., 1977. The oceanic microcosm of particles. Science 198 (4321), 997–1009.

Lam, P.J., Bishop, J.K.B., 2008. The continental margin is a key source of iron to the HNLC North Pacific Ocean. Geophys. Res. Lett 35 (7), http://dx.doi.org/10.1029/2008GL033294.

Lam, P.J., Morris, P.J., 2013. In Situ Marine Sample Collection System and Methods, Patent Pending (13/864,655).

Lam, P.J., Doney, S.C., Bishop, J.K.B., 2011. The dynamic ocean biological pump: Insights from a global compilation of particulate organic carbon, CaCO₃, and opal concentration profiles from the mesopelagic. Glob. Biogeochem. Cycles 25 (3), http://dx.doi.org/10.1029/2010GB003868.

Lam, P.J., Ohnemus, D.C., Marcus, M.A., 2012. The speciation of marine particulate iron adjacent to active and passive continental margins. Geochim. Cosmochim. Acta 80, 108–124.

Lam, P.J., Ohnemus, D.C., Auro, M.E., 2015. Size fractionated major particle composition and mass from the US GEOTRACES North Atlantic Zonal Transect. Deep-Sea Research II: Topical Studies in Oceanography 116, 303–320.

Lambert, C.E., Bishop, J., Biscaye, P.E., Chesselet, R., 1984. Particulate aluminium, iron and manganese chemistry at the deep Atlantic boundary layer. Earth Planet. Sci. Lett. 70 (2), 237–248.

Lima, I.D., Lam, P.J., Doney, S.C., 2013. Dynamics of particulate organic carbon flux in a global ocean model. Biogeosci. Discuss. 10 (9), 14715–14767. http://dx.doi.org/10.5194/bgd-10-14715-2013.

Lisitzin, A.P., 1972. Sedimentation in the World Ocean. Society of Economic Paleontologists and Mineralogists, Tulsa, Okla.

Mahowald, N.M., Baker, A.R., Bergametti, G., Brooks, N., Duce, R.A., Jickells, T.D., Kubilay, N., Prospero, J.M., Tegen, I., 2005. Atmospheric global dust cycle and iron inputs to the ocean. Glob. Biogeochem. Cycles 19 (4), http://dx.doi.org/10.1029/2004GB002402.

Mahowald, N.M., Engelstaedter, S., Luo, C., Sealy, A., Artaxo, P., Benitez-Nelson, C., Bonnet, S., Chen, Y., Chuang, P.Y., Cohen, D.D., Dulac, F., Herut, B., Johansen, A.M., Kubilay, N., Losno, R., Maenhaut, W., Paytan, A., Prospero, J.M., Shank, L.M., Siefert, R.L., 2009. Atmospheric iron deposition: global distribution, variability, and human perturbations. Annu. Rev. Mar. Sci. 1 (1), 245–278. http://dx.doi.org/10.1146/annurev.marine.010908.163727.

Marchal, O., Lam, P.J., 2012. What can paired measurements of Th isotope activity and particle concentration tell us about particle cycling in the ocean? Geochim. Cosmochim. Acta 90(C), 126–148. http://dx.doi.org/10.1016/j.gca.2012.05.009.

McCave, I.N., 1983. Particulate size spectra, behavior, and origin of nepheloid layers over the Nova Scotian continental rise. J. Geophys. Res.: Oceans 88 (C12), 7647–7666.

McCave, I.N., 1984. Size spectra and aggregation of suspended particles in the deep ocean. Deep-Sea Res. A Oceanogr. Res. 31 (4), 329–352.

McCave, I.N., Hall, I.R., 2002. Turbidity of waters over the Northwest Iberian continental margin. Prog. Oceanogr. 52 (2), 299–313.

McDonnell, A.M.P., Buesseler, K.O., 2012. A new method for the estimation of sinking particle fluxes from measurements of the particle size distribution, average sinking velocity, and carbon content. Limnol. Oceangr. Methods 10, 329–346. http://dx.doi.org/10.4319/lom.2012.10.329.

Middag, R., de Baar, H.J.W., Laan, P., Bakker, K., 2009. Dissolved aluminium and the silicon cycle in the Arctic Ocean. Mar. Chem. 115 (3–4), 176–195. http://dx.doi.org/10.1016/j.marchem.2009.08.002.

Moore, J.K., Braucher, O., 2008. Sedimentary and mineral dust sources of dissolved iron to the world ocean. Biogeosciences 5 (3).

Morad, S., Aldahan, A.A., 1986. Alteration of detrital Fe–Ti oxides in sedimentary rocks. Geol. Soc. Am. Bull. 97 (5), 567–578. http://dx.doi.org/10.1130/0016-7606 (1986)97 < 567:AODFOI > 2.0.CO;2.

Moran, S.B., Moore, R.M., 1991. The potential source of dissolved aluminum from resuspended sediments to the North Atlantic Deep Water. Geochim. Cosmochim. Acta 55 (10), 2745–2751.

Murnane, R.J., Cochran, J.K., Buesseler, K.O., Bacon, M.P., 1996. Least-squares estimates of thorium, particle, and nutrient cycling rate constants from the JGOFS North Atlantic Bloom Experiment. Deep-Sea Res. I: Oceanogr. Res. Pap., 239–25843, 239–258.

Murray, R.W., Leinen, M., 1996. Scavenged excess aluminum and its relationship to bulk titanium in biogenic sediment from the central equatorial Pacific Ocean. Geochim. Cosmochim. Acta 60 (20), 3869–3878.

Noble, A.E., Lamborg, C.H., Ohnemus, D.C., Lam, P.J., Goepfert, T.J., Measures, C.I., Frame, C.H., Casciotti, K.L., DiTullio, G.R., Jennings, J., Saito, M.A., 2012. Basin-scale inputs of cobalt, iron, and manganese from the Benguela-Angola front to the South Atlantic Ocean. Limnol. Oceanogr. 57 (4), 989–1010. http://dx.doi.org/10.4319/lo.2012.57.4.0989.

Nolting, R.F., Ramkema, A., Everaarts, J.M., 1999. The geochemistry of Cu, Cd, Zn, Ni and Pb in sediment cores from the continental slope of the Banc d'Arguin (Mauritania). Cont. Shelf Res. 19 (5), 665–691.

Ohnemus, D.C., Auro, M.E., Sherrell, R.M., Lagerström, M., Morton, P.L., Twining, B.S., Rauschenberg, S.M., Lam, P.J., 2014. Laboratory inter-comparison of marine particulate digests including Piranha: a novel chemical method for dissolution of polyethersulfone filters. Limnol. Oceanogr.: Methods (in press).

Pearce, C.I., Qafoku, O., Liu, J., Arenholz, E., Heald, S.M., Kukkadapu, R.K., Gorski, C.A., Henderson, C.M.B., Rosso, K.M., 2012. Synthesis and properties of titanomagnetite ($Fe_{3−x}Ti_xO_4$) nanoparticles: a tunable solid-state Fe (II/III) redox system. J. Colloid Interface Sci. 387 (1), 24–38. http://dx.doi.org/10.1016/j.jcis.2012.06.092.

Petschick, R., Kuhn, G., Gingele, F., 1996. Clay mineral distribution in surface sediments of the South Atlantic: sources, transport, and relation to oceanography. Mar. Geol. 130 (3), 203–229.

Plewa, K., Meggers, H., Kuhlmann, H., Freudenthal, T., Zabel, M., Kasten, S., 2012. Geochemical distribution patterns as indicators for productivity and terrigenous input off NW Africa. Deep-Sea Res. I 66(C), 51–66. http://dx.doi.org/10.1016/j.dsr.2012.04.005.

Prytulak, J., Elliott, T., 2007. TiO₂ enrichment in ocean island basalts. Earth Planet. Sci. Lett. 263 (3), 388–403. http://dx.doi.org/10.1016/j.epsl.2007.09.015.

Ratmeyer, V., Fischer, G., Wefer, G., 1999. Lithogenic particle fluxes and grain size distributions in the deep ocean off northwest Africa: implications for seasonal changes of aeolian dust input and downward transport. Deep-Sea Res. I 46 (8), 1289–1337.

Revels, B.N., Ohnemus, D.C., Lam, P.J., Conway, T.M., John, S.G., 2015. Distribution of particulate Fe and Fe isotopes in the North Atlantic. Deep-Sea Research II: Topical Studies in Oceanography 116, 321–331. http://dx.doi.org/10.1016/j.dsr2.2014.12.004.

Rognon, P., Gaussen, G.C., Revel, M., Grousset, F.E., Pedemay, P., 1996. Holocene Saharan dust deposition on the Cape Verde Islands: sedimentological and Nd–Sr isotopic evidence. Sedimentology 43 (2), 359–366.

Rothe, P., 1973. Sedimentation in the deep-sea areas adjacent to the Canary and Cape Verde Islands. Mar. Geol. 14 (3), 191–206.

Rudnick, R.L., Gao, S., 2003. Composition of the continental crust. Treatise Geochem. 3, 1–64.

Rutgers van der Loeff, M., Boudreau, B.P., 1997. The effect of resuspension on chemical exchanges at the sediment-water interface in the deep sea—a modelling and natural radiotracer approach. J. Mar. Syst..

Schlitzer, R., 2013. Ocean Data View, 2013. Available from: ⟨http://odv.awi.de⟩.

Schott, F., Stommel, H., 1978. Beta spirals and absolute velocities in different oceans. Deep-Sea Res. 25 (11), 961–1010.

Severmann, S., Mcmanus, J., Berelson, W.M., Hammond, D.E., 2010. The continental shelf benthic iron flux and its isotope composition. Geochim. Cosmochim. Acta 74 (14), 3984–4004. http://dx.doi.org/10.1016/j.gca.2010.04.022.

Shelley, R., et al., 2015. Title TBA (in review). Deep-Sea Res. II: Top. Oceanogr. 116, 262–272. http://dx.doi.org/10.1016/j.dsr2.2014.12.005.

Sherrell, R., Boyle, E., 1992. The trace metal composition of suspended particles in the oceanic water column near Bermuda. Earth Planet. Sci. Lett. 111 (1), 155–174.

Stuut, J.-B., 2005. Provenance of present-day eolian dust collected off NW Africa. J. Geophys. Res. 110 (D4), http://dx.doi.org/10.1029/2004JD005161.

Taylor, S.R., McLennan, S.M., 1995. The geochemical evolution of the continental crust. Rev. Geophys. 33 (2), 241–265.

Ternon, E., Guieu, C., Loÿe-Pilot, M.-D., Leblond, N., Bosc, E., Gasser, B., Miquel, J.-C., Martín, J., 2010. The impact of Saharan dust on the particulate export in the water column of the North Western Mediterranean Sea. Biogeosciences 7 (3), 809–826.

Vrieling, E., Poort, L., Beelen, T., Gieskes, W., 1999. Growth and silica content of the diatoms *Thalassiosira weissflogii* and *Navicula salinarum* at different salinities and enrichments with aluminium. Eur. J. Phycol. 34 (3), 307–316. http://dx.doi.org/10.1080/09670269910001736362.

Yücel, M., Konovalov, S.K., Moore, T.S., Janzen, C.P., Luther III, G.W., 2010. Chem. Geol. 269 (3–4), 364–375. http://dx.doi.org/10.1016/j.chemgeo.2009.10.010.

Zabel, M., Bickert, T., Dittert, L., Haese, R.R., 1999. Significance of the sedimentary Al:Ti ratio as an indicator for variations in the circulation patterns of the equatorial North Atlantic. Paleoceanography 14 (6), 789–799.